Broadband Cross Polarization to Half-Integer Quadrupolar Nuclei: Wideline Static NMR Spectroscopy

James J. Kimball[1,2], Adam R. Altenhof[1,2], Michael J. Jaroszewicz[3], and Robert W. Schurko[1,2,*]

1. Department of Chemistry & Biochemistry, Florida State University, Tallahassee, FL 32306

2. National High Magnetic Field Laboratory, Tallahassee, FL 32310

3. Department of Chemical & Biological Physics, Weizmann Institute of Science, Rehovot, Israel 7610001

*Author to whom correspondence should be addressed

E-mail: rschurko@fsu.edu

Abstract

Cross polarization (CP) is a technique commonly used for the signal enhancement of NMR spectra; however, applications to quadrupolar nuclei have heretofore been limited due to a number of problems, including poor spin locking efficiency, inconvenient relaxation times, and reduced CP efficiencies over broad spectral bandwidths – this is unfortunate, since they constitute 73% of NMR-active nuclei in the Periodic Table. The Broadband Adiabatic Inversion Cross Polarization (BRAIN-CP) pulse sequence has proven useful for the signal enhancement of wideline and ultra-wideline (*i.e.*, 250 kHz to several MHz in breadth) powder patterns arising from stationary samples; however, a comprehensive investigation of its application to half-integer quadrupolar nuclei (HIQN) is currently lacking. Herein, we present theoretical and experimental considerations for the application of BRAIN-CP for the acquisition of central-transition (CT, $+1/2 \leftrightarrow -1/2$) powder patterns of HIQN. Consideration is given to parameters crucial to the success of the experiment, such as the Hartmann-Hahn (HH) matching conditions and the phase modulation of the contact pulse. Modifications to the BRAIN-CP sequence such as flip-back pulses (FB) and ramped contact pulses applied to the ^{1}H spins are used for the reduction of experimental times and increased CP bandwidth capabilities, respectively. Spectra for a series of quadrupolar nuclei with broad CT powder patterns, including ^{35}Cl ($S = 3/2$), ^{55}Mn ($S = 5/2$), ^{59}Co ($S = 7/2$), and ^{93}Nb ($S = 9/2$), are acquired via direct excitation (CPMG and WCPMG) and indirect excitation (CP/CPMG and BRAIN-CP) methods. We demonstrate that proper implementation of the sequence can enable ^{1}H-*S* broadband CP over a bandwidth of 1 MHz, which, to the best of our knowledge, is the largest CP bandwidth reported to date. Finally, we establish the basic principles necessary for simplified optimization and execution of the BRAIN-CP pulse sequences for a wide range of HIQN.

1. Introduction

Since its introduction over fifty years ago, cross polarization (CP)[1–3] has become arguably the most important technique in solid-state NMR (SSNMR) spectroscopy. This is largely due to the substantial signal enhancements and experimental time reductions it affords via the transfer of nuclear spin polarization from abundant to dilute spins, as well as its use in investigating and exploiting the spatial proximity of dipolar-coupled nuclei.[4–9] As such, the CP pulse sequence motif is a standard building block in numerous pulse sequences that are applied for the study of a wide range of solid materials. The majority of publications featuring CP overwhelmingly report its use in tandem with magic-angle spinning (MAS),[10] and largely focus on CP between spin-1/2 nuclei (^{1}H→^{13}C and ^{1}H→^{15}N CP/MAS NMR experiments are by far the most widely reported).[11–13] CP involving integer and half-integer spin quadrupolar nuclei has been explored to a much lesser degree.[14–19] This is in part due to non-optimal relaxation times (*e.g.*, $T_{1\rho}$, the rotating frame longitudinal relaxation time, and/or T_{IS}, the cross-relaxation time),[2,20,21] reduced spin locking efficiency (especially under MAS),[22–24] and the complexities of broadband CP in experiments featuring spectra with wideline patterns arising from anisotropic quadrupolar interactions.[25,26]

SSNMR spectra of half-integer quadrupolar nuclei (HIQN) are influenced by the quadrupolar interaction (QI), as defined by the quadrupolar coupling constant, $C_Q = eQV_{33}/h$ (in Hz), and the asymmetry parameter, $\eta_Q = (V_{11} - V_{22})/V_{33}$ (dimensionless), where V_{11}, V_{22}, and V_{33} are the principal components of the electric field gradient (EFG) tensor, ordered such that $|V_{11}| \leq |V_{22}| \leq |V_{33}|$. The central transition (CT, $+1/2 \leftrightarrow -1/2$) pattern is influenced only by the second order QI (SOQI), whereas the satellite transition (STs, other $\Delta m = \pm 1$ transitions) patterns are broadened by both the first-order (FOQI) and SOQI.[27–29] The manifestation of C_Q in CT and ST

patterns is determined by the quadrupolar frequency, $\omega_Q = 2\pi\nu_Q = 3C_Q/[2\pi(2I(2I-1))]$, η_Q, and the orientation dependences of the FOQI and the SOQI, where pattern broadening scales proportional to ω_Q and ω_Q^2/ω_0, respectively. As such, CT patterns have much smaller breadths than those of ST patterns. Nevertheless, for most HIQN in the periodic table, the CT patterns can have breadths from 5 kHz to 250 kHz (wideline NMR spectra), or even 250 kHz to tens of MHz (ultra-wideline (UW) spectra).[30,31]

The use of MAS is of limited use for the acquisition of UWNMR spectra, and in particular, UW CT patterns of HIQN. While current state-of-the-art technology allows for spinning rates of > 100 kHz,[32] these are not sufficient for the complete averaging of first-order anisotropic interactions in many cases (*i.e.*, chemical shift anisotropy, homonuclear dipolar coupling, and the FOQI). Furthermore, the SOQI is unique in that it is only partially averaged by fixed angle spinning experiments.[33,34] Thus, the UW CT patterns of many HIQN acquired under MAS display severe anisotropic broadening with significant overlap between the isotropic centerband and spinning side bands.

The large breadths of UWNMR powder patterns lead to two main problems: (i) UWNMR powder patterns inherently have low SNRs, and (ii) the efficiency of conventional methods for acquisition of UWNMR spectra is compromised, primarily due to the limited bandwidths of rectangular pulses for excitation, refocusing, and polarization transfer. Pulse sequences aimed at increasing SNRs for both direct excitation (*i.e.*, Carr-Purcell Meiboom Gill, CPMG)[35–37] and indirect excitation (*i.e.*, CP) often fall short for the acquisition of UWNMR patterns due to their implicit use of rectangular pulses. The well-known solution to these problems is the implementation of frequency swept (FS) pulses. Analogs of the CPMG and CP experiments that use FS pulses (notably, wideband uniform-rate smooth-truncation (WURST) pulses),[38] including

WURST-CPMG (WCPMG for short)[39,40] and Broadband Adiabatic-Inversion Cross Polarization (BRAIN-CP/WCPMG, BRAIN-CP for short),[41] have found widespread use for the acquisition of UWNMR spectra via direct excitation (DE) and broadband CP, respectively.

While the potential gain in signal from CP remains a lucrative option for HIQN, it is notoriously challenging to achieve under MAS. This is primarily due to the inability to efficiently spin-lock CT magnetization relative to analogous static experiments.[22–24,42] There is a complex dependence of the spin locking efficiency on the relative magnitudes of the QI (ω_Q), the amplitude of the spin locking pulse (ω_1), and the spinning rate (ω_{rot}), where only when the adiabaticity parameter, α, is greater than 1, permit for efficient CP (*i.e.*, $\alpha \approx \omega_1/(\omega_{rot}\omega_Q) > 1$);[22] however, even this is not always a reliable determinant.[43,44] Furthermore, anisotropic nutation behavior across the breadth of the CT pattern can occur, resulting in distorted powder patterns.[45,46]

Herein, we demonstrate the application of the BRAIN-CP pulse sequence for the acquisition of CT powder patterns of HIQN under static conditions, featuring broadband CP from spin-1/2 nuclei to HIQN (*i.e.*, $I \rightarrow S$). Though there are several examples of BRAIN-CP for HIQN,[47–49] a comprehensive experimental and theoretical investigation has not been reported (in contrast to those for spin-1/2 or integer-spin quadrupolar nuclei). [26,41] An analytical formulation of the Hartmann-Hahn (HH) matching conditions utilizing WURST pulse irradiation for the *S* spins is described. A combination of numerical and analytical simulations are used to monitor the mechanisms underlying CP, spin-locking, and storage of spin polarization along the $+z$ and/or $-z$ axes; all of these offer insight into the optimal parameterization of the BRAIN-CP sequence for application to HIQN. Spectra are acquired using DE (CPMG and WCPMG) and CP (CP/CPMG and BRAIN-CP) methods for a series of HIQN featuring different QIs and nuclear

spin numbers, including ^{35}Cl (S = 3/2), ^{55}Mn (S = 5/2), ^{59}Co (S = 7/2), and ^{93}Nb (S = 9/2), in order to draw comparisons between methods. Consideration is also given to modifications of the BRAIN-CP pulse sequence aimed at the reduction of experimental times (*e.g.*, flip-back (FB) ^{1}H pulses) and the improvement of the quadrupolar pattern uniformity (ramped ^{1}H contact pulses). Finally, we discuss the ease of implementation of the BRAIN-CP sequence for acquiring UWNMR spectra of HIQN, and the great potential of this methodology for increasing SSNMR exploration of a wide range of nuclei from elements across the Periodic Table.

2. Experimental Methods

2.1. Samples

Glycine HCl (Sigma Aldrich), cyclopentadienylmanganese(I)tri-carbonyl (η^5-$CpMn(CO)_3$, Sigma Aldrich), chloropentaaminecobalt(III)chloride ($[Co(NH_3)_5Cl]Cl_2$, Alfa Aesar), cyclopentadienylniobium(V)tetrachloride ($CpNbCl_4$, STREM Chemicals, Inc.) were purchased from the listed sources and used in all subsequent NMR experiments without further purification. All samples were ground into fine powders on the benchtop under ambient conditions and were packed into 5 mm polychlorotrifluoroethylene (PCTFE) sample holders with Viton o-rings designed at NHMFL and machined by Shenzhen Rapid Direct Co., Ltd.

2.2. SSNMR Spectroscopy

SSNMR spectra were acquired using a Bruker Avance NEO console and a 14.1 T Magnex/Bruker [ν_0 (^{1}H) = 600 MHz] wide bore magnet at resonance frequencies of ν_0 (^{35}Cl) = 58.787 MHz, ν_0 (^{55}Mn) = 148.735 MHz, ν_0 (^{59}Co) = 142.363 MHz, and ν_0 (^{93}Nb) = 146.857 MHz. A home-built 5 mm double-resonance (HX) probe was used for all experiments. All data

were collected under stationary conditions (*i.e.*, non-rotating samples). Spectra were acquired with ^{1}H continuous wave (CW) decoupling with RF fields of 50 kHz. Chemical-shift reference frequencies were calibrated using the following standards: (i) ^{35}Cl reference: NaCl (*s*) with δ_{iso} = 0.0 ppm;[50] (ii) ^{55}Mn reference: 1.0 M $KMnO_4$ (*aq*) with δ_{iso} = 0.0 ppm;[51] (iii) ^{59}Co reference: 0.1 M $K_3Co(CN)_6$ (*aq*) with δ_{iso} = 0.0 ppm;[51] and (iv) ^{93}Nb reference: saturated $NbCl_5$ in acetonitrile with δ_{iso} = 0.0 ppm.[52,53] RF pulse powers for all samples were calibrated by arraying the excitation pulse width in CPMG experiments (see **Supplement S1**).

In all CP experiments, calibrated spin-locking fields applied to the *S* and *I* spins, $\nu_{1,S}$ and $\nu_{1,I}$, were set between $\nu_{1,S}$ = 2 - 25 kHz and $\nu_{1,I}$ = 12.5 - 50 kHz. In conventional CP experiments, the optimal experimental Hartmann-Hahn (HH) matching conditions were chosen as the ratio of RF powers on the *S* and *I* channels yielding spectra with patterns of the highest signal intensity. In BRAIN-CP experiments, the HH match was set based on the abovementioned criterion, as well as optimal pattern uniformity (*i.e.*, patterns most resembling the ideal powder pattern, with minimal distortions). A full listing of all parameters is given in the Supporting Information, **Tables S1** - **S4**. All direct-excitation (DE) schemes employ the eight-step phase cycling scheme used by Bhattacharyya and Frydman.[54] All CP schemes use the sixteen-step phase cycling scheme used by Larsen and co-workers.[35] All pulse sequences described herein are available via https://github.com/rschurko.

2.3. Spectral Processing and Simulations

All data sets were processed in MATLAB via the coaddition of echoes, convolution with a gaussian function, fast-Fourier transform, and magnitude calculation (*i.e.*, the spectra are not phased) using a custom-written code (available on request). Numerical simulations were

performed with the *Spinach* 2.6 open source software package.[55] All CP spin dynamics were simulated using an ABCX spin system with one $S = 3/2$ nucleus and three ^{1}H nuclei. The coordinates of the spin system are based on those from the DFT-D2* refined crystal structure of glycine HCl.[56] The spin system interactions are limited to quadrupolar, heteronuclear dipolar, and homonuclear dipolar only. Chemical shift interactions for all spins are ignored for simplicity. For numerical simulations, distinct values of C_Q are used, with η_Q set to zero in all cases. This allows for description of the orientation of the largest component of the EFG tensor, V_{33}, with respect to the magnetic field, $\mathbf{B}_0$, by just one angle: β (the azimuthal angle, α, is undefined since $V_{11} = V_{22}$). In the case of $\eta_Q = 0$, groups of nuclear spins sharing the same β have identical resonance frequencies in the rotating frame and are referred to herein as *isochromats*. Numerical simulations of powder patterns made use of the Zaremba-Conroy-Wolfsburg (ZCW) powder averaging scheme[57,58] with 28,656 orientations. Calculations were performed on a MacBook Pro operating on macOS 13.1 with an Apple M1 Pro chip and on NMRBox virtual machines.[59]

3. Results and Discussion

3.1. Overview

Here, we discuss the development and application of BRAIN-CP methods for the acquisition of static SSNMR spectra of four HIQN: ^{35}Cl ($S = 3/2$), ^{55}Mn ($S = 5/2$), ^{59}Co ($S = 7/2$), and ^{93}Nb ($S = 9/2$). These nuclei and their respective samples represent a series of different nuclear spin numbers and distinct quadrupolar interactions, which are ideal for demonstrating the versatility and effectiveness of the BRAIN-CP pulse sequence (**Scheme 1**) for the acquisition of UWNMR spectra of HIQN. First, practical considerations for experimental optimization of the BRAIN-CP pulse sequence for the acquisition of SSNMR spectra of HIQN are discussed (**§3.2**).

Then, it is demonstrated how BRAIN-CP can be used to acquire high-quality UWNMR spectra of CT patterns for the aforementioned nuclei (**§3.3** - **3.6**). In each case, spectra obtained with CPMG, WCPMG, CP/CPMG, and BRAIN-CP pulse sequences (see **Scheme S1** for descriptions of these sequences) are compared, and assessed in terms of *spectral quality* (*i.e.*, relative signal intensity and pattern uniformity). Lastly, we discuss several tenets that emerge from this work, which can aid in the facile implementation of the BRAIN-CP sequence for the exploration of a range of systems containing half-integer-spin quadrupolar nuclei from across the Periodic Table.

3.2. Practical Considerations

Polarization transfer afforded by the BRAIN-CP experiment can be maximized by the optimization of three key parameters in the pulse sequence: (i) the maximum amplitude of the contact pulse ($\omega_{1,S}$), (ii) the sweep width (Δ), and (iii) the contact time (τ_{CT}). The latter two parameters are used to define the phase modulation of the BRAIN contact pulse and are in general sample dependent (*i.e.*, determined by factors such as the identity of the target nucleus and the magnitude of the quadrupolar interaction), and are also related to the sweep rate ($R = \Delta/\tau_{CT}$, in kHz ms^{-1}). In the sections that follow, these parameters are given consideration in the context of Hartmann-Hahn matching, optimal sweep widths and contact times, and distortions appearing in the CT power patterns of stationary samples featuring HIQN with large quadrupolar interactions.

3.2.1. Hartmann-Hahn Matching

The amplitude of the contact pulse in the BRAIN-CP experiment should be chosen to simultaneously satisfy two conditions: (i) to establish the HH match and (ii) to adiabatically spin lock the spin polarization produced from CP as the effective field, $\mathbf{B}_{\text{eff}}$, sweeps from $\pm z$ to $\mp z$ (the sign of the spin polarization at the end of the contact pulse depends on the sweep direction and the phase of the initial pulse on the ^{1}H channel, see **Figure S3**). The latter condition is less stringent than the former and has been thoroughly explored.[60–62] In general, adiabatic spin locking involves the controlled application of the $\mathbf{B}_1$ field to ensure that the spins precess about $\mathbf{B}_{\text{eff}}$ at a constant rate in a state of quasi-equilibrium, without loss of polarization. This can be achieved with WURST pulses using varying amplitudes and sweep rates. Nevertheless, WURST pulses with very low amplitudes or very fast sweep rates tend to cause the spin polarization to behave in a non-adiabatic manner.

The generalized HH matching condition is also well understood[5] (an analytical derivation of the HH matching condition is given in **Supplement S2**); however, key points regarding the manner in which it is established for BRAIN-CP to HIQN are discussed in the ensuing text. Provided that (i) $\omega_{1,S} \ll \omega_Q$, where $\omega_{1,S} = 2\pi\nu_{1,S} = -\gamma_S B_{1,S}$ is the amplitude of the S spin-locking pulse, and (ii) Δ is greater than the pattern breadth (see **§3.2.2**), the HH match for each isochromat occurs at different points in time (herein referred to as the *instantaneous HH match*) when

$$\omega_{1,I} = \omega_{e,S}(t, \beta) \qquad (1)$$

where $\omega_{1,I} = 2\pi\nu_{1,I} = -\gamma_I B_{1,I}$ is the proton spin locking amplitude, $\omega_{e,S}(t,\beta)$ is the effective RF field of a WURST pulse applied to the S spins, and β is the angle between the direction of V_{33} and $\mathbf{B}_0$.

The effective frequency in a frame that rotates synchronously with the phase modulation $\varphi(t)$ (*i.e.,* the frequency modulated frame) is described as:

$$\omega_{e,S}(t,\beta) = \sqrt{\left(\Omega_S + \omega_Q^{(2)}(\beta) - \omega_p(t)\right)^2 + \left((S+1/2)\cdot\omega_{1,S}\cdot A(t)\right)^2} \quad (2)$$

where $\Omega_S = \omega_{0,S} - \omega_{RF,S}$ is the transmitter offset (where $\omega_{0,S}$ is the resonance frequency in the laboratory frame and $\omega_{RF,S}$ is the time-independent transmitter frequency), $\omega_p(t) = d\varphi(t)/dt$ is the instantaneous (*i.e.*, time-dependent) transmitter frequency arising from the phase modulation, $\varphi(t) = \pm 2\pi\{(\Delta/2)t - (\Delta/2\tau_{CT})t^2\}$, and $A(t) = 1 - |\cos(\pi t/\tau_{CT})|^N$ is the amplitude modulation of the contact pulse, respectively (here, N is an integer, commonly set to 2, 20, or 80).[61] Assuming an axially symmetric EFG tensor (*i.e.*, $\eta_Q = 0$), the second order quadrupolar frequency for the $m_S \leftrightarrow m_S - 1$ transition is defined as[63]

$$\omega_Q^{(2)}(\beta) = \frac{\omega_Q^2}{12\omega_0}(3/2)\sin^2(\beta)\left[(A+B)\cos^2(\beta) - B\right]$$

where A and B are defined as:

$$A = 24m_S(m_S-1) - 4S(S+1) + 9$$

$$B = (1/4)[6m_S(m_S-1) - 2S(S+1) + 3]$$

Analytical and numerical simulations can provide insight into the time-dependent CP processes that occur during the contact pulse (**Fig. 1**). Analytical simulations (**Figs. 1c** and **1d**)) involve plotting $\omega_{e,S}(t,\beta)/2\pi = \nu_{e,S}(t,\beta)$ according to Eq. (2) and $\omega_{1,I}/2\pi = \nu_{1,I}$ as a function of the contact time for two different EFG tensor orientations, $\beta = \pi/4$ and $\beta = \pi/2$, which correspond to isochromats with resonance frequencies at the low- and high-frequency edges of the powder pattern (**Figs. 1a** and **1b**), respectively, arising from different second-order quadrupolar shifts, $\omega_Q^{(2)}(\beta)$. Intersections between $\nu_{e,S}(t,\beta)$ (red line) and $\nu_{1,I}$ (blue line) indicate the predicted HH

matching conditions. The regions between 45 kHz and 55 kHz are highlighted in light blue and are representative of the broadening of the matching conditions due to the hetero- and homonuclear dipolar interactions.[7] The vertical dashed lines denote the time in which CP is predicted to occur and are used for comparisons to numerical simulations. Numerical simulations in *Spinach* for a four-spin system (see **§2.3**) are used to calculate the expectation values of $\langle \mathbf{I}_x \rangle$ and $\langle \mathbf{S}_z^{(2\text{-}3)} \rangle$ for the $\beta = \pi/2$ and $\beta = \pi/4$ isochromats (**Figs. 1e** and **1f**), which describe the trajectories of the *I* and *S* spin polarizations, respectively, during the contact time. The operator $\langle \mathbf{S}_z^{(2\text{-}3)} \rangle$ is a fictitious spin-1/2 operator[64,65] describing the polarization of the (2-3) subspace (*i.e.*, the population difference between the $1/2 \leftrightarrow -1/2$ states). Polarization transfer events are evidenced by simultaneous decreases in $\langle \mathbf{I}_x \rangle$ and increases in $\langle \mathbf{S}_z^{(2\text{-}3)} \rangle$. The following sets of parameters are used for analytical and numerical simulations: $C_Q = 6.5$ MHz and $\eta_Q = 0$ (corresponding to a ^{35}Cl CT pattern with a breadth of 90 kHz at 14.1 T); the proton spin locking amplitude, $\nu_{1,I} = 50$ kHz; the quadrupolar spin locking amplitude, $\nu_{1,S} = 25$ kHz; the sweep width, $\Delta = 175$ kHz; the contact time, $\tau_{CT} = 20$ ms (see **§3.2.2** for discussion of the parameterization of Δ and τ_{CT}); and the transmitter offset, $\Omega_S/2\pi = -15$ kHz (corresponding to the center of gravity of the powder pattern).

The analytical and numerical simulations are first compared for the $\beta = \pi/4$ isochromat (low-frequency edge of the pattern). The analytical simulation (**Fig. 1c**) predicts a matching condition in the region between *ca.* 3 and 7 ms, as that is the time during which $\nu_{e,S}(t, \beta = \pi/4)$ is between 45 and 55 kHz. At the start of the numerical simulation (**Fig. 1e**, bottom row), $\langle \mathbf{I}_x \rangle = 1$ and $\langle \mathbf{S}_z^{(2\text{-}3)} \rangle = 0$. The phase modulation of the contact pulse and the initial phase of the starting density matrix are set such that the effective frequency sweeps from low to high frequency, resulting in magnetization buildup along the $+z$ axis (**Fig. S3**).[26,41] The simultaneous increase in

$\langle \mathbf{S}_z^{(2\text{-}3)} \rangle$ and decrease in $\langle \mathbf{I}_x \rangle$ is indicative of a CP event that occurs within the time frame predicted by the analytical simulation. The continued buildup of $\langle \mathbf{S}_z^{(2\text{-}3)} \rangle$ between *ca*. 7 and 20 ms is indicative of efficient spin locking by the time- and orientation-dependent $\mathbf{B}_{\text{eff}}$ (*i.e.*, $\omega_{e,S}(t, \beta = \pi/4)$). The oscillations observed in the plot of $\langle \mathbf{S}_z^{(2\text{-}3)} \rangle$ arise from multiple heteronuclear dipolar couplings.[66]

The second case ($\beta = \pi/2$ isochromat) shows similar behaviour, both analytically and numerically. The analytical expression for the effective frequency (**Fig. 1d**) is a mirror image of that of the $\beta = \pi/4$ isochromat, as the resonance frequencies of the isochromats are equidistant from Ω_S in opposite directions. Since the resonance frequency of the $\beta = \pi/2$ isochromat is at the high-frequency edge of the powder pattern, its predicted matching conditions occur much later in the contact time period compared to those of the $\beta = \pi/4$ isochromat, between *ca*. 12 and 17.5 ms, as the pulse is swept from low to high frequency. Numerical simulations predict the CP event timing to match well with that in the analytical simulation (**Fig. 1f**), as the decrease in $\langle \mathbf{I}_x \rangle$ and increase in $\langle \mathbf{S}_z^{(2\text{-}3)} \rangle$ occur within the region indicated by the dotted lines, wherein $\nu_{e,S}$ (t, $\beta=\pi/2$) ≈ 45 - 55 kHz.

While Eqn. (2) provides an accurate prediction of the HH matching conditions for different groups of spin isochromats, it is informative for the experimentalist to consider the conditions required for the match to be satisfied for all isochromats. These conditions are realizable so long as the sweep width, Δ, of the contact pulse is chosen such that it is greater than the pattern breadth (*vide infra*). This allows for the instantaneous frequency to be equal to the shift of each isochromat relative to the transmitter offset at some point in time during the pulse [*i.e.*, $\omega_{\text{p}}(t) = \Omega_S + \omega_{\text{Q}}^{(2)}(\beta)$]. As a result, the first squared term in Eq. (2), $(\Omega_S + \omega_{\text{Q}}^{(2)}(\beta) - \omega_p(t))$, is zero for each isochromat as its matching condition occurs. Therefore, the matching

condition which allows for maximum polarization transfer to all isochromats across the entire powder pattern can be approximated as:

$$\omega_{1,I} \approx (S + 1/2) \cdot \omega_{1,S} \quad (3)$$

which is similar to the HH matching condition that has been established for CP from spin-1/2 to HIQN.[42,67] It is emphasized that while the spin dynamics do follow Eq. (2), Eq. (3) is provided solely for practical purposes (*i.e.*, facile determination of an initial HH match).

3.2.2. Phase Modulation of the Contact Pulse

In order to achieve broadband CP, consideration must be given to the two parameters used to define the phase modulation of the contact pulse: the sweep width, Δ, and the contact time, τ_{CT}. The value of Δ yielding the highest CP enhancement depends on the NMR characteristics of the target HIQN (*S* and *eQ*), the quadrupolar parameters (C_Q and η_Q), and the magnitude of $\mathbf{B}_0$, since these together determine the CT pattern breadth. In order to adiabatically spin lock isochromats across the entire breadth of a powder pattern, Δ must be larger than that of the pattern breadth.[62,68,69] Experimental results (and numerical simulations, see **Fig. S4** and discussion below) suggest that the value of Δ resulting in maximum polarization transfer is between 1.5 and 2 times the breadth of the intended powder pattern (*vide infra*). Larger sweeps unnecessarily shorten the time during which the instantaneous HH match is met for each isochromat, which can decrease the CP efficiency. While the pattern breadth also has a large influence on the choice of τ_{CT}, careful consideration must also be given to the γ of the HIQN (*vide infra*). The rate of cross relaxation during CP scales directly with the magnitude of the heteronuclear dipolar coupling;[3,20,21] therefore, τ_{CT} must be chosen to allow for sufficient CP at

each instantaneous HH match. It is noted that relaxation can also determine the choice of τ_{CT} in the limit of short $T_{1\rho}$ time constants for both *I* and *S* spins.

Numerical simulations are used to gain insight into the dependency of polarization buildup on the length of τ_{CT} during BRAIN-CP experiments, with consideration given to the magnitude of the heteronuclear dipolar couplings (**Fig. S4**, **Fig. 2**). As in previous simulations, a four-spin system is used (see **§2.3**). This time however, the identity of the *S* nucleus and the magnitude of C_Q are adjusted to represent systems with heteronuclear dipolar couplings of varying magnitudes and powder patterns of increasing breadths, respectively. The two *S* nuclei used are ^{35}Cl and ^{75}As, both spin-3/2, with $\gamma(^{75}\text{As}) \approx 1.75\gamma(^{35}\text{Cl})$, engendering a proportional difference in heteronuclear dipolar coupling constants [*i.e.*, $R_{DD}(^{75}\text{As}, ^{1}\text{H}) \approx 1.75R_{DD}(^{35}\text{Cl}, ^{1}\text{H})$]. At 14.1 T, $C_Q(^{35}\text{Cl})$ values of 6.5, 9.6, and 13.5 MHz correspond to CT patterns of *ca*. 100, 200, and 400 kHz in breadth, respectively. $C_Q(^{75}\text{As})$ values of 8.5, 12.8, and 18 MHz correspond to CT patterns of comparable breadths to those in the ^{35}Cl series (all values of $\eta_Q = 0$). The following experimental parameters are used: $\nu_{1,I} = 50$ kHz; Δ is set to *ca*. 1.5 times the pattern breadth; $\Omega_S/2\pi$ is set to the center of gravity of the pattern (–15, –30, –120 kHz for patterns of 100, 200, and 400 kHz, respectively).

For all six examples, the value of $\langle \mathbf{S}_z^{(2\text{-}3)} \rangle$ for the $\beta = \pi/2$ isochromat at the end of the BRAIN-CP pulse is plotted in **Figure 2** as a function of increasing values of τ_{CT}. The CP enhancement is associated with the breadth of the pattern, as maximum $\langle \mathbf{S}_z^{(2\text{-}3)} \rangle$ is obtained only for the narrower patterns. The diminished CP buildup observed with increasing pattern breadths is attributed to the shortening of the instantaneous matching conditions as the contact pulse sweeps across larger frequency ranges. This decrease in CP efficiency with larger pattern breadths (and accordingly larger frequency sweeps) is more pronounced in the ^{35}Cl examples,

further illustrating the need for long contact times when acquiring the spectrum at one transmitter offset, especially when polarizing samples with low-γ nuclei and/or weak heteronuclear dipolar couplings.

The application of long contact pulses with high rf amplitudes in BCP experiments is normally not an option, since modern solid-state NMR probes have a range of limiting duty cycles; for example, for typical solids probes, pulse sequences using solely high-frequency pulses (*e.g.*, ^{1}H, ^{19}F; 50-300 W) have lower duty cycles than those using solely low-frequency pulses (*e.g.*, ^{13}C and lower-γ nuclei; 200-400 W).[70,71] Therefore, a balance between long contact times and higher rf amplitudes must be struck (fortunately, the WURST-based contact pulses often function well with low rf fields, *vide infra*). Furthermore, to exploit the effective transverse relaxation (T_2^{eff}) characteristics to maximize the signal obtained from CPMG or WURST-CPMG experiments, high-power ^{1}H decoupling is often applied to hydrogen-rich samples over the entire course of the echo acquisition train to reduce the impact of dipolar transverse relaxation mechanisms,[72,73] which further adds to the duty cycle. Hence, for nuclei with moderate values of γ, we have found that contact times between 10 to 20 ms are usually sufficient; however, as discussed above, systems with low heteronuclear dipolar couplings may benefit from or necessitate longer contact times.

3.2.3. Pattern Distortions

Altenhof *et al*. and Hansen *et al*. previously reported "dips" in the CT patterns of spectra of HIQN with axially symmetric EFG tensors (*i.e.*, distortions away from pattern uniformity in localized frequency regions).[74–76] This is attributed to the transfer of polarization between multiple Zeeman states for EFG tensor orientations with β at or near 54.74°. Isochromats

corresponding to these orientations have similar resonance frequencies for the CT and STs (*i.e.*, degenerate or nearly degenerate Zeeman levels in a frame that rotates at $\omega_0 + \omega_Q^{(1)}(\beta) + \omega_Q^{(2)}(\beta)$, herein referred to as the *rotating quadrupolar frame* (RQF), making selective manipulation of the CT via RF pulses difficult. Upon irradiation of these isochromats, spin polarization is distributed amongst the different Zeeman levels and a pronounced "dip" in the CT powder pattern is often observed. However, this effect is not unique to systems with axially symmetric EFG tensors. As detailed in **Supplement S3**, regardless of the value of η_Q, certain isochromats have nearly degenerate Zeeman levels in the RQF, making such dips ubiquitous in CT patterns of HIQN. However, these distortions are most prominent in systems with $\eta_Q = 0$, as the quadrupolar frequency only depends on the angle β, meaning that the resonance frequencies of isochromats with degenerate Zeeman levels are all similar. In cases of non-axially symmetric EFG tensors ($\eta_Q \neq 0$), the resonance frequencies of isochromats with degenerate Zeeman levels can occur across the entire frequency range of the powder pattern, and thus, the polarization loss is not localized to a specific subset of frequencies. We emphasize that while these distortions can result in powder patterns that deviate from the ideal pattern shapes, they usually do not hinder the extraction of accurate EFG and CS tensor parameters.

3.3. ^{35}Cl SSNMR experiments

Glycine HCl is an ideal test sample for making comparisons between spectra acquired with DE and CP experiments and exploring the effects of different parameters in the BRAIN-CP pulse sequence: its ^{35}Cl static NMR spectrum features a wideline CT pattern (*ca*. 150 kHz in breadth at 14.1 T) that is primarily influenced by the SOQI, the $T_1(^1H)$ and $T_1(^{35}Cl)$ are both small (allowing for short recycle delays in both DE and CP experiments), and the high natural

abundance of ^{35}Cl and high wt-% of chlorine in the sample both enable fast acquisition.[77,78] Spectra acquired with the CPMG and CP/CPMG pulse sequences using standard rectangular pulses are compared to those acquired with the WCPMG and BRAIN-CP pulse sequences featuring FS pulses (**Fig. 3**). We note that because of inherent differences between WURST and rectangular pulses, quantitative comparisons of signal intensities are only made between BRAIN-CP and WCPMG spectra and CP/CPMG and CPMG spectra, respectively.[79] All spectra were acquired with 16 transients and optimized recycle times of 1 s and 2 s for DE and CP experiments, respectively (see **Tables S1** - **S4** for a listing of all experimental parameters). The CPMG sequence, as applied, yields signal across the breadth of the powder pattern; however, the intensities near the pattern edges are reduced due to the bandwidth limitations of the rectangular pulses (**Fig. 3a**). CP/CPMG provides large signal enhancement yet, the frequency bandwidth over which CP occurs is substantially less than the total pattern breadth (**Fig. 3b**). By contrast, the WURST pulses in WCPMG yield a uniform powder pattern (**Fig. 3c**) that matches the ideal pattern. Finally, the BRAIN-CP sequence allows for acquisition of a powder pattern with high S/N that closely resembles the ideal lineshape (**Fig. 3d**). Using a spin locking pulse of $\nu_{1I} = 50$ kHz, the predicted HH match from **Eqn. 3** is $\nu_{1S} = 25$ kHz. Experimentally we find a similar match of $\nu_{1S} = 19.9$ kHz.

Of the four nuclei investigated herein, ^{35}Cl presents a unique case due to its low γ. The heteronuclear dipolar couplings of this sample are significantly lower than those of the others, which in turn means significantly slower rates of cross relaxation during CP in the former (*vide supra*). As discussed above (**§3.2.2**), the lengthening of the instantaneous HH match via long BRAIN-CP contact pulses is instrumental in achieving optimal CP. Unsurprisingly, the contact time required to achieve maximum CP enhancement in BRAIN-CP is significantly longer than

that required in CP/CPMG. Spectra acquired with CP/CPMG and BRAIN-CP using contact times ranging from 5 to 25 ms are compared in **Fig. 4**. Contact times between 10 to 20 ms result in maximum signal enhancement using CP/CPMG, whereas the integrated intensity of the spectra acquired with BRAIN-CP continues to increase with increasing contact times. We note that while the integrated intensities of powder patterns acquired with CP/CPMG are higher than those acquired with BRAIN-CP at lower contact times(as is typically the case due to the much longer time frame during which polarization transfer is allowable in the former), the CP bandwidths are limited for the former.

3.4. ^{55}Mn SSNMR experiments

A comparison of the ^{55}Mn static NMR spectra of η^5-CpMn(CO)$_3$ acquired at 14.1 T with the four different pulse sequences is shown in **Fig. 5**. The ideal CT powder pattern has a breadth of *ca*. 1 MHz at 14.1 T, primarily due to second-order quadrupolar broadening arising from the large quadrupolar interaction (C_Q(^{55}Mn) = 64.3 MHz).[80] The DE CPMG spectrum, which was acquired with short, high-power pulses (*i.e.*, $\tau_{\pi/2}^{sel}$ = 1.3 μs), features signal over the entire breadth of the powder pattern (but with significant distortions), demonstrating the bandwidth limitations of rectangular pulses (**Fig. 5a**). As in the case of the ^{35}Cl NMR experiments, CP/CPMG only allows for acquisition of a small portion of the total powder pattern (**Fig. 5b**). Acquisition of the powder pattern with WCPMG using excitation and refocusing pulses of low rf amplitudes results in a spectrum with a uniform powder pattern of high S/N, though with clear departures from ideality between –700 and –800 kHz (**Fig. 5c**). The presence of these "dips" is more readily observed here than in the ^{35}Cl NMR spectra (**Fig. 3**) due to the higher spin number of ^{55}Mn (giving rise to more STs) and the lower η_Q value (isochromats with $\beta \approx 54.74°$ for which

this phenomenon occur all have similar resonance frequencies). Finally, the spectrum acquired using BRAIN-CP with a ramped ^{1}H spin-locking pulse ($\nu_{1,I}$ is ramped linearly from 37 to 57 kHz) also features the entire pattern (**Fig. 5d**), though with lower S/N (note the scaling factor of 4) and reduced uniformity than that in **Fig. 5c**.

Several observations can be drawn from these results. First, the DE experiments outperform the CP experiments, regardless of the use of rectangular or WURST pulses. The poorer CP performance is likely due to the short $T_1(^{55}\text{Mn}) \approx 28$ ms (**Fig. S5**, and correspondingly short $T_{1\rho}(^{55}\text{Mn})$), which prohibits the use of a longer contact time (which would likely be beneficial in the BRAIN-CP experiment, given the breadth of the pattern). Nevertheless, to the best of our knowledge, this is the first report of CP across a bandwidth of 1 MHz at a single transmitter offset. It is noted that all ^{1}H-^{55}Mn CP experiments included flip-back (FB) pulses on the ^{1}H channel due to the long $T_1(^{1}\text{H})$ time constant ($T_1(^{1}\text{H}) \approx 225$ s, as estimated from an optimized recycle delay of 45 s),[81,82] serving to reduce experimental times by more than a factor of 2 (**Fig. S6**).

Second, acquisition of an increasingly uniform powder pattern using BRAIN-CP is achieved by linearly ramping $\nu_{1,I}$, which serves to compensate for non-uniform amplitudes $\nu_{1,S}$ at offset frequencies far from the transmitter (**Fig. S8-S12**). Spectra acquired using BRAIN-CP at different spin locking amplitudes, $\nu_{1,S}$, are displayed in **Fig. 6**. If the ^{1}H spin-locking power is held constant at $\nu_{1,I} = 40$ kHz (**Fig. 6a**), optimal CP occurs at different amplitudes of $\nu_{1,S}$ (as indicated by the areas of highest intensity shown in blue and violet), inferring that obtaining a uniform power pattern is not possible at a single setting for $\nu_{1,S}$. For instance, the spectrum acquired using $\nu_{1,S} = 11.5$ kHz (indicated by the dashed line) is displayed above the contour plot, where pattern intensity is amplified at the high frequency edge. In **Fig. 6b**, $\nu_{1,I}$ was ramped from

ca. 36 to 57 kHz, with all other conditions identical to those in **Fig. 6a**. In this instance, the matching conditions occur at similar amplitudes, allowing for the acquisition of a spectrum with a powder pattern of improved uniformity (though not perfect), as evidenced by the spectrum also acquired using $\nu_{1,S}$ = 11.5 kHz displayed above the contour plot. The modulation of $\nu_{1,I}$ adds an additional time dependence to the HH matching conditions and thus reduces the reliability of Eq. 3 for an accurate prediction of the HH match. However, if $\nu_{1,I}$ is approximated as its average over the course of the total contact time (46.5 kHz), the match is predicted to occur at $\nu_{1,S}$ = 15.5 kHz, which is close the experimentally determined value of $\nu_{1,S}$ = 11.5 kHz. We note that non-uniform amplitude profiles affect other BRAIN-CP experiments on UWNMR patterns in a similar manner (**Fig. S7**). However, for patterns of lesser breadths, ^{1}H spin-locking pulses of constant rf amplitude are sufficient for providing CP enhancement across the entire powder pattern with minimal distortions. Explorations of other options for modulations of the ^{1}H and/or *S* RF amplitudes (and possibly phases) are beyond the scope of the current work, though this is something our group is currently exploring.

Finally, for systems with small $T_1(S)$ and large $T_1(I)$ time constants, the BRAIN-CP experiment generally produces a spectrum with a lower SNR relative to that of DE WCPMG; however, there is still great value in the former for revealing connectivities between spin-1/2 and quadrupolar nuclei, and also for potential use in dynamic nuclear polarization (DNP) NMR experiments,[83,84] which when conducted via transfer of spin polarization from e^- to ^{1}H to *S* nuclei, where the spectrum of the *S* nucleus features a broad pattern, would require efficient ^{1}H-*S* broadband CP.[47,85]

3.5. ^{59}Co SSNMR experiments

^{59}Co (S = 7/2) static SSNMR spectra often feature CT patterns that are affected by both anisotropic chemical shift and quadrupolar interactions.[86–89] ^{59}Co static NMR spectra of $[Co(NH_3)_5Cl]Cl_2$ acquired at 14.1 T using CPMG, CP/CPMG, WCPMG, and BRAIN-CP are presented in **Fig. 7**, along with the ideal simulation of the CT pattern, which spans *ca*. 300 kHz (again, ^{1}H FB pulses were used in the CP experiments). The moderate γ and high spin number of ^{59}Co, along with the moderate CSAs and C_Q magnitudes, allow for acquisition of the complete powder pattern using CPMG (**Fig. 7a**). In the CP/CPMG spectrum (**Fig. 7b**), the powder pattern intensity is higher than that in the CPMG spectrum, though only over a reduced frequency range near the transmitter. The use of FS pulses in WCPMG and BRAIN-CP (**Fig. 7c** and **7d**) allow for acquisition of UW powder patterns of high SNR, with significant CP enhancement in the latter. Given a spin locking power of $\nu_{1,I}$ = 50 kHz, Eqn. (3) predicts the BRAIN-CP HH match to occur at $\nu_{1,S}$ = 12.5 kHz. Experimentally, the match is found to occur at ν_{1S} = 9.1 kHz. All spectra feature CT patterns with a significant "dip" in intensity just to the low-frequency side of their centers, which is a result of polarization transfer from the CT to the STs (*vide supra*). In comparison to the analogous set of ^{55}Mn spectra (**Fig. 5**), the dips are more pronounced here, which is due to the increased overlap of the CT pattern and multiple ST patterns resulting from both the higher nuclear spin quantum number and reduced C_Q. Furthermore, the dip is more apparent in **Fig. 7d** relative to that in **Fig. 7c**, since CP to these isochromats is less efficient due to small or negligible dipolar interactions (*N.B.*: similar effects are observed in ^{1}H-^{55}Mn CP experiments).[90]

^{59}Co SSNMR spectra acquired with CP and BRAIN-CP using different RF powers and corresponding HH matching conditions are compared in **Fig. 8**. The bandwidth over which

conventional CP operates decreases with increasing nuclear spin quantum numbers. This comes as a direct result of the dependency of the HH match condition on the nuclear spin number (*vide supra*). Typically, the maximum allowable $\nu_{1,I}$ (due to probe limitations) is in the tens of kHz regime, meaning $\nu_{1,S}$ can be as low as several kHz for nuclei with high spin quantum numbers. The CP bandwidth in conventional CP depends directly on $\nu_{1,S}$, and thus, the bandwidth diminishes significantly with decreasing amplitudes (**Fig. 8**, top row). By contrast, the CP bandwidth in BRAIN-CP experiments covers the entire breadth of the pattern, even at low RF amplitudes (**Fig. 8**, bottom row). The diminished intensity in the spectrum acquired with the lowest RF amplitudes (**Fig. 8c**, bottom row) is likely the result of diminished adiabatic spin-locking on both channels (*i.e.*, small $\mathbf{B}_{\text{eff}}$ fields). Of great importance here is that experiments with low RF amplitudes ($\nu_{1,S}$) may permit increased contact times, thereby being of great value for low-γ nuclei, while also minimizing damage and wear to probes resulting from the continuous application of high-power pulses.

3.6. ^{93}Nb SSNMR experiments

As a final test of the applicability of these pulse sequences to HIQN, ^{93}Nb static SSNMR experiments were conducted on a sample of $CpNbCl_4$, which has a CT pattern that spans *ca*. 200 kHz at 14.1 T.[91] As for the ^{59}Co case above, a spectrum displaying a uniform powder pattern is acquired at one transmitter offset using CPMG (**Fig. 9a**), only a fraction of the pattern is observed using CP/CPMG (**Fig. 9b**), and both WCPMG (**Fig. 9c**) and BRAIN-CP (**Fig. 9d**) allow for acquisition of spectra with high-quality powder patterns using pulses with low rf amplitudes. Eq. (3) predicts the HH match to occur at $\nu_{1,S}$ = 10 kHz, whereas the experimentally determined match is $\nu_{1,S}$ = 8 kHz. Due to the high spin number (S = 9/2) and high η_Q value of

0.83, both spectra acquired using DE methods display some signal intensity at both edges of the CT patterns which originates from the STs (**Fig. 9a**, **9c**), as indicated by the ideal lineshape of the STs which fall within the experimental spectral window displayed above **Fig. 9c**. The spectrum acquired using BRAIN-CP does not share these features, resulting in a CT powder pattern that cleanly terminates at the high-frequency discontinuity. This is attributed to the different matching conditions between the CT and the other STs based on their respective nutation frequencies. This feature exemplifies a form of spectral editing as it can aid in the precise extraction of the quadrupolar tensor parameters in cases where direct-excitation methods fail in selective acquisition of the CT. As in the case of ^{55}Mn, the lower intensity of the spectrum acquired with BRAIN-CP relative to the other spectra is attributed to a short $T_1(^{93}\text{Nb})$ (**Fig. S5**) and therefore short $T_{1\rho}(^{93}\text{Nb})$.

4. Conclusions

In this work, it is shown how the BRAIN-CP pulse sequence can be used for the acquisition of UWNMR spectra of HIQN in stationary samples, yielding spectra with high SNRs and uniform CT patterns. The spin dynamics describing CP between the spin-1/2 nuclei and HIQN are explained using a combination of analytical and numerical simulations.

General recommendations for pulse sequence parameters: The HH match for BRAIN-CP to HIQN can be approximated as $\omega_{1I} \approx (S + 1/2)\omega_{1S}$, so long as the sweep width of the contact pulse is greater than the pattern breadth – this tenet makes facile the setup and optimization of the experiment. Optimal sweep widths are between 1.5 and 2.0 times the breadth of the target powder pattern. Contact times of 10 ms or less are generally sufficient for the CP enhancement of wideline patterns of nuclei with moderate to high values of γ. Low-γ nuclei and/or nuclei

exhibiting UW powder patterns necessitate the use of longer contact times in order to achieve optimal CP enhancement. While most patterns feature noticeable distortions due to polarization loss from the CT, these effects are understood, can be accurately modeled (*i.e.*, simulated), and in most cases do not interfere with the extraction of accurate EFG (and CS) tensor parameters. The inclusion of ^{1}H FB and ramped contact pulses can aid in the reduction of experimental length and the improvement of pattern uniformity in the acquisition of UWNMR powder patterns, respectively, though we will continue to explore other options for making these improvements via amplitude and/or phase modulations and the *I* and *S* channels. The samples investigated herein feature nuclei of different spin quantum numbers, quadrupolar interactions with varying magnitudes, and a range of different gyromagnetic ratios; hence, the successful acquisition of their respective ^{1}H-*S* BRAIN-CP spectra demonstrate the robustness of this sequence. We expect that these methods will positively impact UWNMR investigations of very unreceptive HIQN, and perhaps find future use with modern DNP methods to aid in the routine study of heretofore under-investigated nuclei.

Declaration of Competing Interest

The authors declare that they have no known competing financial interests or personal relationships that could have appeared to influence the work reported in this paper.

Acknowledgements

R.W.S. and J.J.K would like to thank the National Science Foundation Chemical Measurement and Imaging Program, with partial co-funding from the Solid State and Materials Chemistry Program (NSF-2003854), for supporting this work. Significant portions of this work were also funded by the Basic Energy Sciences Program in the Department of Energy (DE-SC0022310). The National High Magnetic Field Laboratory is supported by the National Science Foundation (NSF/DMR-1644779, NSF/DMR-2128556) and the State of Florida. This study made use of NMRbox: National Center for Biomolecular NMR Data Processing and Analysis, a Biomedical Technology Research Resource (BTRR), which is supported by NIH grant P41GM111135 (NIGMS). J.J.K. and R.W.S. would like to thank Dr. Frederic Mentink-Vigier for his helpful discussions on spin dynamics and numerical simulations.

Supporting Information

Pulse sequence schematics, NMR acquisition parameters, additional SSNMR spectra, additional numerical simulations.

References

(1) Hartmann, S. R.; Hahn, E. L. Nuclear Double Resonance in the Rotating Frame. *Phys. Rev.* **1962**, *128*, 2042–2053. https://doi.org/10.1103/PhysRev.128.2042.

(2) Pines, A.; Gibby, M. G.; Waugh, J. S. Proton-Enhanced Nuclear Induction Spectroscopy. A Method for High Resolution NMR of Dilute Spins in Solids. *J. Chem. Phys.* **1972**, *56*, 1776–1777. https://doi.org/10.1063/1.1677439.

(3) Pines, A.; Gibby, M. G.; Waugh, J. S. Proton-Enhanced NMR of Dilute Spins in Solids. *J. Chem. Phys.* **1973**, *59*, 569–590. https://doi.org/10.1063/1.1680061.

(4) Kolodziejski, W.; Klinowski, J. Kinetics of Cross-Polarization in Solid-State NMR: A Guide for Chemists. *Chem. Rev.* **2002**, *102*, 613–628. https://doi.org/10.1021/cr000060n.

(5) Rovnyak, D. Tutorial on Analytical Theory for Cross-Polarization in Solid State NMR. *Concepts Magn. Reson. Part A Bridg. Educ. Res.* **2008**, *32A*, 254–276. https://doi.org/10.1002/cmr.a.

(6) Smith, M. E. Recent Progress in Solid-State NMR of Spin-½ Low-γ Nuclei Applied to Inorganic Materials. *Phys. Chem. Chem. Phys.* **2022**. *59*, 864-907. https://doi.org/10.1039/D2CP03663K.

(7) Marks, D.; Vega, S. A Theory for Cross-Polarization NMR of Nonspinning and Spinning Samples. *J. Magn. Reson. Ser. A* **1996**, *118*, 157–172. https://doi.org/10.1006/jmra.1996.0024.

(8) Schmidt-Rohr, K.; Spiess, H. W. *Multidimensional Solid-State NMR and Polymers*; Elsevier, **1994**. https://doi.org/10.1016/C2009-0-21335-3.

(9) Levitt, M. H.; Suter, D.; Ernst, R. R. Spin Dynamics and Thermodynamics in Solid-State NMR Cross Polarization. *J. Chem. Phys.* **1986**, *84*, 4243–4255. https://doi.org/10.1063/1.450046.

(10) Andrew, E. R.; Bradbury, A.; Eades, R. G. Nuclear Magnetic Resonance Spectra from a Crystal Rotated at High Speed. *Nature* **1958**, *182*, 1659–1659. https://doi.org/10.1038/1821659a0.

(11) Schaefer, J.; Stejskal, E. O. Carbon-13 Nuclear Magnetic Resonance of Polymers Spinning at the Magic Angle. *J. Am. Chem. Soc.* **1976**, *98*, 1031–1032. https://doi.org/10.1021/ja00420a036.

(12) Stejskal, E.; Schaefer, J.; Waugh, J. Magic-Angle Spinning and Polarization Transfer in Proton-Enhanced NMR. *J. Magn. Reson.* **1977**, *28*, 105–112. https://doi.org/10.1016/0022-2364(77)90260-8.

(13) Hong, M.; Yao, X.; Jakes, K.; Huster, D. Investigation of Molecular Motions by Lee-Goldburg Cross-Polarization NMR Spectroscopy. *J. Phys. Chem. B* **2002**, *106*, 7355–7364. https://doi.org/10.1021/jp0156064.

(14) Bryant, R. G.; Ganapathy, S.; Kennedy, S. D. High-Resolution Calcium-43 NMR in Solids. *J. Magn. Reson.* **1987**, *72*, 376–378. https://doi.org/10.1016/0022-2364(87)90303-9.

(15) Harris, R. K.; Nesbitt, G. J. Cross Polarization for Quadrupolar Nuclei—Proton to Sodium-23. *J. Magn. Reson.* **1988**, *78*, 245–256. https://doi.org/10.1016/0022-2364(88)90268-5.

(16) Morris, H. D.; Bank, S.; Ellis, P. D. Aluminum-27 NMR Spectroscopy of Iron-Bearing Montmorillonite Clays. *J. Phys. Chem.* **1990**, *94*, 3121–3129. https://doi.org/10.1021/j100370a069.

(17) Edwards, J. C.; Ellis, P. D. Cross-Polarization for Quadrupolar Nuclei—Proton to Molybdenum-95. *Magn. Reson. Chem.* **1990**, *28*, S59–S67. https://doi.org/10.1002/mrc.1260281312.
(18) Lim, K. H.; Grey, C. P. 19F/23Na Multiple Quantum Cross Polarization NMR in Solids. *J. Chem. Phys.* **2000**, *112*, 7490–7504. https://doi.org/10.1063/1.481347.
(19) Barrie, P. J. Distorted Powder Lineshapes in 27Al CP / MAS NMR Spectroscopy of Solids. *Chem. Phys. Lett.* **1993**, *208*, 486–490. https://doi.org/10.1016/0009-2614(93)87177-5.
(20) Demco, D. E.; Tegenfeldt, J.; Waugh, J. S. Dynamics of Cross Relaxation in Nuclear Magnetic Double Resonance. *Phys. Rev. B* **1975**, *11*, 4133–4151. https://doi.org/10.1103/PhysRevB.11.4133.
(21) Vega, S. Multiple-Quantum Cross-Polarization NMR on Spin Systems with I = 1/2 and S=3/2 in Solids. *Phys. Rev. A* **1981**, *23*, 3152–3173. https://doi.org/10.1103/PhysRevA.23.3152.
(22) Vega, A. J. MAS NMR Spin Locking of Half-Integer Quadrupolar Nuclei. *J. Magn. Reson.* **1992**, *96*, 50–68. https://doi.org/10.1016/0022-2364(92)90287-H.
(23) Ashbrook, S. E.; Wimperis, S. Spin-Locking of Half-Integer Quadrupolar Nuclei in Nuclear Magnetic Resonance of Solids: Creation and Evolution of Coherences. *J. Chem. Phys.* **2004**, *120*, 2719–2731. https://doi.org/10.1063/1.1638995.
(24) Ashbrook, S. E.; Wimperis, S. Spin-Locking of Half-Integer Quadrupolar Nuclei in Nuclear Magnetic Resonance of Solids: Second-Order Quadrupolar and Resonance Offset Effects. *J. Chem. Phys.* **2009**, *131,* 194509. https://doi.org/10.1063/1.3263904.
(25) Harris, K. J.; Veinberg, S. L.; Mireault, C. R.; Lupulescu, A.; Frydman, L.; Schurko, R. W. Rapid Acquisition of 14N Solid-State NMR Spectra with Broadband Cross Polarization. *Chem. - A Eur. J.* **2013**, *19*, 16469–16475. https://doi.org/10.1002/chem.201301862.
(26) Altenhof, A. R.; Wi, S.; Schurko, R. W. Broadband Adiabatic Inversion Cross-polarization to Integer-spin Nuclei with Application to Deuterium NMR. *Magn. Reson. Chem.* **2021**, *59*, 1009–1023. https://doi.org/10.1002/mrc.5145.
(27) Kentgens, A. P. M. A Practical Guide to Solid-State NMR of Half-Integer Quadrupolar Nuclei with Some Applications to Disordered Systems. *Geoderma* **1997**, *80*, 271–306. https://doi.org/10.1016/S0016-7061(97)00056-6.
(28) Ashbrook, S. E. Recent Advances in Solid-State NMR Spectroscopy of Quadrupolar Nuclei. *Phys. Chem. Chem. Phys.* **2009**, *11*, 6892-6905. https://doi.org/10.1039/b907183k.
(29) Vega, A. J. Quadrupolar Nuclei in Solids. In *Encyclopedia of Magnetic Resonance*; John Wiley & Sons, Ltd: Chichester, UK, 2010. https://doi.org/10.1002/9780470034590.emrstm0431.pub2.
(30) Schurko, R. W. Acquisition of Wideline Solid-State NMR Spectra of Quadrupolar Nuclei. In *Encyclopedia of Magnetic Resonance*; John Wiley & Sons, Ltd: Chichester, UK, 2011. https://doi.org/10.1002/9780470034590.emrstm1199.
(31) Schurko, R. W. Ultra-Wideline Solid-State NMR Spectroscopy. *Acc. Chem. Res.* **2013**, *46* (9), 1985–1995. https://doi.org/10.1021/ar400045t.
(32) Paruzzo, F. M.; Walder, B. J.; Emsley, L. Line Narrowing in 1H NMR of Powdered Organic Solids with TOP-CT-MAS Experiments at Ultra-Fast MAS. *J. Magn. Reson.* **2019**, *305*, 131–137. https://doi.org/10.1016/j.jmr.2019.06.015.
(33) Kundla, E.; Samoson, A.; Lippmaa, E. High-Resolution NMR of Quadrupolar Nuclei in

Rotating Solids. *Chem. Phys. Lett.* **1981**, *83*, 229–232. https://doi.org/10.1016/0009-2614(81)85451-6.
(34) Medek, A.; Harwood, J. S.; Frydman, L. Multiple-Quantum Magic-Angle Spinning NMR: A New Method for the Study of Quadrupolar Nuclei in Solids. *J. Am. Chem. Soc.* **1995**, *117*, 12779–12787. https://doi.org/10.1021/ja00156a015.
(35) Larsen, F. H.; Jakobsen, H. J.; Ellis, P. D.; Nielsen, N. C. Sensitivity-Enhanced Quadrupolar-Echo NMR of Half-Integer Quadrupolar Nuclei. Magnitudes and Relative Orientation of Chemical Shielding and Quadrupolar Coupling Tensors. *J. Phys. Chem. A* **1997**, *101*, 8597–8606. https://doi.org/10.1021/jp971547b.
(36) Siegel, R.; Nakashima, T. T.; Wasylishen, R. E. Sensitivity Enhancement of NMR Spectra of Half-Integer Quadrupolar Nuclei in the Solid State via Population Transfer. *Concepts Magn. Reson. Part A* **2005**, *26A*, 47–61. https://doi.org/10.1002/cmr.a.20037.
(37) Hung, I.; Rossini, A. J.; Schurko, R. W. Application of the Carr−Purcell Meiboom−Gill Pulse Sequence for the Acquisition of Solid-State NMR Spectra of Spin- 1/2 Nuclei. *J. Phys. Chem. A* **2004**, *108*, 7112–7120. https://doi.org/10.1021/jp0401123.
(38) Kupce, Ē.; Freeman, R. Optimized Adiabatic Pulses for Wideband Spin Inversion. *J. Magn. Reson. Ser. A* **1996**, *118*, 299–303. https://doi.org/10.1006/jmra.1996.0042.
(39) O'Dell, L. A.; Schurko, R. W. QCPMG Using Adiabatic Pulses for Faster Acquisition of Ultra-Wideline NMR Spectra. *Chem. Phys. Lett.* **2008**, *464*, 97–102. https://doi.org/10.1016/j.cplett.2008.08.095.
(40) O'Dell, L. A.; Rossini, A. J.; Schurko, R. W. Acquisition of Ultra-Wideline NMR Spectra from Quadrupolar Nuclei by Frequency Stepped WURST–QCPMG. *Chem. Phys. Lett.* **2009**, *468*, 330–335. https://doi.org/10.1016/j.cplett.2008.12.044.
(41) Harris, K. J.; Lupulescu, A.; Lucier, B. E. G.; Frydman, L.; Schurko, R. W. Broadband Adiabatic Inversion Pulses for Cross Polarization in Wideline Solid-State NMR Spectroscopy. *J. Magn. Reson.* **2012**, *224*, 38–47. https://doi.org/10.1016/j.jmr.2012.08.015.
(42) Amoureux, J.-P.; Pruski, M. Theoretical and Experimental Assessment of Single- and Multiple-Quantum Cross-Polarization in Solid State NMR. *Mol. Phys.* **2002**, *100*, 1595–1613. https://doi.org/10.1080/00268970210125755.
(43) Sun, W.; Stephen, J. T.; Potter, L. D.; Wu, Y. Rotation-Induced Resonance and Second-Order Quadrupolar Effects on Spin Locking of Half-Integer Quadrupolar Nuclei. *J. Magn. Reson. Ser. A* **1995**, *116*, 181–188. https://doi.org/10.1006/jmra.1995.0006.
(44) De Paul, S. M.; Ernst, M.; Shore, J. S.; Stebbins, J. F.; Pines, A. Cross-Polarization from Quadrupolar Nuclei to Silicon Using Low-Radio-Frequency Amplitudes during Magic-Angle Spinning. *J. Phys. Chem. B* **1997**, *101*, 3240–3249. https://doi.org/10.1021/jp9623711.
(45) Ding, S. W.; Mcdowell, C. A. Theoretical Calculations of the CPMAS Spectral Lineshapes of Half-Integer Quadrupole Systems. *J. Magn. Reson. Ser. A* **1995**, *114*, 80–87. https://doi.org/10.1006/jmra.1995.1108.
(46) Ding, S. W.; Mcdowell, C. A. Nutation Magic-Angle-Spinning Spectra of Half-Integer Quadrupole Spin Systems. *J. Magn. Reson. Ser. A* **1995**, *112*, 36–42. https://doi.org/10.1006/jmra.1995.1007.
(47) Hirsh, D. A.; Rossini, A. J.; Emsley, L.; Schurko, R. W. 35Cl Dynamic Nuclear Polarization Solid-State NMR of Active Pharmaceutical Ingredients. *Phys. Chem. Chem. Phys.* **2016**, *18*, 25893–25904. https://doi.org/10.1039/c6cp04353d.

(48) Laurencin, D.; Ribot, F.; Gervais, C.; Wright, A. J.; Baker, A. R.; Campayo, L.; Hanna, J. V.; Iuga, D.; Smith, M. E.; Nedelec, J.-M.; et. al. 87Sr, 119Sn, 127I Single and {1H/19F}-Double Resonance Solid-State NMR Experiments: Application to Inorganic Materials and Nanobuilding Blocks. *ChemistrySelect* **2016**, *1*, 4509–4519. https://doi.org/10.1002/slct.201600805.
(49) Namespetra, A. M.; Hirsh, D. A.; Hildebrand, M. P.; Sandre, A. R.; Hamaed, H.; Rawson, J. M.; Schurko, R. W. 35Cl Solid-State NMR Spectroscopy of HCl Pharmaceuticals and Their Polymorphs in Bulk and Dosage Forms. *CrystEngComm* **2016**, *18*, 6213–6232. https://doi.org/10.1039/C6CE01069E.
(50) Gee, M.; Wasylishen, R. E.; Laaksonen, A. A More Reliable Absolute Shielding Scale for Chlorine: Combined Experimental and Theoretical Approach. *J. Phys. Chem. A* **1999**, *103*, 10805–10812. https://doi.org/10.1021/jp9925841.
(51) Harris, R. K.; Becker, E. D.; Cabral De Menezes, S. M.; Goodfellow, R.; Granger, P. NMR Nomenclature: Nuclear Spin Properties and Conventions for Chemical Shifts (IUPAC Recommendations 2001). *Concepts Magn. Reson.* **2002**, *14*, 326–346. https://doi.org/10.1002/cmr.10035.
(52) Papulovskiy, E.; Shubin, A. A.; Terskikh, V. V.; Pickard, C. J.; Lapina, O. B. Theoretical and Experimental Insights into Applicability of Solid-State 93Nb NMR in Catalysis. *Phys. Chem. Chem. Phys.* **2013**, *15*, 5115-5131. https://doi.org/10.1039/c3cp44016h.
(53) Deblonde, G. J. P.; Coelho-Diogo, C.; Chagnes, A.; Cote, G.; Smith, M. E.; Hanna, J. V.; Iuga, D.; Bonhomme, C. Multinuclear Solid-State NMR Investigation of Hexaniobate and Hexatantalate Compounds. *Inorg. Chem.* **2016**, *55*, 5946–5956. https://doi.org/10.1021/acs.inorgchem.6b00345.
(54) Bhattacharyya, R.; Frydman, L. Quadrupolar Nuclear Magnetic Resonance Spectroscopy in Solids Using Frequency-Swept Echoing Pulses. *J. Chem. Phys.* **2007**, *127*, 194503. https://doi.org/10.1063/1.2793783.
(55) Hogben, H. J.; Krzystyniak, M.; Charnock, G. T. P.; Hore, P. J.; Kuprov, I. Spinach – A Software Library for Simulation of Spin Dynamics in Large Spin Systems. *J. Magn. Reson.* **2011**, *208*, 179–194. https://doi.org/10.1016/j.jmr.2010.11.008.
(56) Holmes, S. T.; Engl, O. G.; Srnec, M. N.; Madura, J. D.; Quiñones, R.; Harper, J. K.; Schurko, R. W.; Iuliucci, R. J. Chemical Shift Tensors of Cimetidine Form A Modeled with Density Functional Theory Calculations: Implications for NMR Crystallography. *J. Phys. Chem. A* **2020**, *124*, 3109–3119. https://doi.org/10.1021/acs.jpca.0c00421.
(57) Zaremba, S. K. Good Lattice Points, Discrepancy, and Numerical Integration. *Ann. di Mat. Pura ed Appl.* **1966**, *73*, 293–317. https://doi.org/10.1007/BF02415091.
(58) Conroy, H. Molecular Schrödinger Equation. VIII. A New Method for the Evaluation of Multidimensional Integrals. *J. Chem. Phys.* **1967**, *47*, 5307–5318. https://doi.org/10.1063/1.1701795.
(59) Maciejewski, M. W.; Schuyler, A. D.; Gryk, M. R.; Moraru, I. I.; Romero, P. R.; Ulrich, E. L.; Eghbalnia, H. R.; Livny, M.; Delaglio, F.; Hoch, J. C. NMRbox: A Resource for Biomolecular NMR Computation. *Biophys. J.* **2017**, *112*, 1529–1534. https://doi.org/10.1016/j.bpj.2017.03.011.
(60) Garwood, M.; DelaBarre, L. The Return of the Frequency Sweep: Designing Adiabatic Pulses for Contemporary NMR. *J. Magn. Reson.* **2001**, *153*, 155–177. https://doi.org/10.1006/jmre.2001.2340.
(61) O'Dell, L. A. The WURST Kind of Pulses in Solid-State NMR. *Solid State Nucl. Magn.*

Reson. **2013**, *55–56*, 28–41. https://doi.org/10.1016/j.ssnmr.2013.10.003.
(62) Van Veendaal, E.; Meier, B. H.; Kentgens, A. P. M. Frequency Stepped Adiabatic Passage Excitation of Half-Integer Quadrupolar Spin Systems. *Mol. Phys.* **1998**, *93*, 195–213. https://doi.org/10.1080/002689798169212.
(63) Schurko, R. W.; Jaroszewicz, M. J. Solid-State NMR of the Light Main Group Metals. In *Encyclopedia of Inorganic and Bioinorganic Chemistry*; John Wiley & Sons, Ltd: Chichester, UK, 2015; pp 1–56. https://doi.org/10.1002/9781119951438.eibc2293.
(64) Vega, S.; Pines, A. Operator Formalism for Double Quantum NMR. *J. Chem. Phys.* **1977**, *66*, 5624–5644. https://doi.org/10.1063/1.433884.
(65) Vega, S. Fictitious Spin 1/2 Operator Formalism for Multiple Quantum NMR. *J. Chem. Phys.* **1978**, *68*, 5518–5527. https://doi.org/10.1063/1.435679.
(66) Luy, B.; Glaser, S. J. Single-Shot Experiments for the Acquisition of Coherence- Transfer Functions in Real Time. *J. Magn. Reson.* **1999**, *138*, 187–190. https://doi.org/10.1006/jmre.1999.1728.
(67) Vega, A. J. CP/MAS of Quadrupolar S=3/2 Nuclei. *Solid State Nucl. Magn. Reson.* **1992**, *1*, 17–32. https://doi.org/10.1016/0926-2040(92)90006-U.
(68) Tannús, A.; Garwood, M. Adiabatic Pulses. *NMR Biomed.* **1997**, *10*, 423–434. https://doi.org/10.1002/(SICI)1099-1492(199712)10:8<423::AID-NBM488>3.0.CO;2-X.
(69) Haase, J.; Conradi, M. S.; Grey, C. P.; Vega, A. J. Population Transfers for NMR of Quadrupolar Spins in Solids. *J. Magn. Reson. Ser. A* **1994**, *109*, 90–97. https://doi.org/10.1006/jmra.1994.1138.
(70) Doty, F. D. Probe Design and Construction. In *Encyclopedia of Magnetic Resonance*; John Wiley & Sons, Ltd: Chichester, UK, 2007; pp 1–19. https://doi.org/10.1002/9780470034590.emrstm1000.
(71) Fukushima, E.; Roeder, S. B. W. *Experimental Pulse NMR: A Nuts and Bolts Approach*; Addison- Wesley Publishing Company, Inc.: Reading, MA, **1981**. https://doi.org/10.1201/9780429493867.
(72) Rossini, A. J.; Mills, R. W.; Briscoe, G. A.; Norton, E. L.; Geier, S. J.; Hung, I.; Zheng, S.; Autschbach, J.; Schurko, R. W. Solid-State Chlorine NMR of Group IV Transition Metal Organometallic Complexes. *J. Am. Chem. Soc.* **2009**, *131*, 3317–3330. https://doi.org/10.1021/ja808390a.
(73) Veinberg, S. L.; Friedl, Z. W.; Harris, K. J.; O'Dell, L. A.; Schurko, R. W. Ultra-Wideline 14 N Solid-State NMR as a Method for Differentiating Polymorphs: Glycine as a Case Study. *CrystEngComm* **2015**, *17*, 5225–5236. https://doi.org/10.1039/C5CE00060B.
(74) Altenhof, A. R.; Lindquist, A. W.; Foster, L. D. D.; Holmes, S. T.; Schurko, R. W. On the Use of Frequency-Swept Pulses and Pulses Designed with Optimal Control Theory for the Acquisition of Ultra-Wideline NMR Spectra. *J. Magn. Reson.* **2019**, *309*, 106612. https://doi.org/10.1016/j.jmr.2019.106612.
(75) Koppe, J.; Hansen, M. R. Minimizing Lineshape Distortions in Static Ultra-Wideline Nuclear Magnetic Resonance of Half-Integer Spin Quadrupolar Nuclei. *J. Phys. Chem. A* **2020**, *124*, 4314–4321. https://doi.org/10.1021/acs.jpca.0c03658.
(76) Hung, I.; Altenhof, A. R.; Schurko, R. W.; Bryce, D. L.; Han, O. H.; Gan, Z. Field-stepped Ultra-wideline NMR at up to 36 T: On the Inequivalence between Field and Frequency Stepping. *Magn. Reson. Chem.* **2021**, *59*, 951–960. https://doi.org/10.1002/mrc.5128.
(77) Bryce, D. L.; Sward, G. D.; Adiga, S. Solid-State 35/37 Cl NMR Spectroscopy of

Hydrochloride Salts of Amino Acids Implicated in Chloride Ion Transport Channel Selectivity: Opportunities at 900 MHz. *J. Am. Chem. Soc.* **2006**, *128*, 2121–2134. https://doi.org/10.1021/ja057253i.

(78) Altenhof, A. R.; Jaroszewicz, M. J.; Harris, K. J.; Schurko, R. W. Broadband Adiabatic Inversion Experiments for the Measurement of Longitudinal Relaxation Time Constants. *J. Chem. Phys.* **2021**, *154* (3). https://doi.org/10.1063/5.0039017.

(79) Veinberg, S. L.; Lindquist, A. W.; Jaroszewicz, M. J.; Schurko, R. W. Practical Considerations for the Acquisition of Ultra-Wideline 14N NMR Spectra. *Solid State Nucl. Magn. Reson.* **2017**, *84*, 45–58. https://doi.org/10.1016/j.ssnmr.2016.12.008.

(80) Ooms, K. J.; Feindel, K. W.; Terskikh, V. V.; Wasylishen, R. E. Ultrahigh-Field NMR Spectroscopy of Quadrupolar Transition Metals: 55Mn NMR of Several Solid Manganese Carbonyls. *Inorg. Chem.* **2006**, *45*, 8492–8499. https://doi.org/10.1021/ic0608445.

(81) Tegenfeldt, J.; Haeberlen, U. Cross Polarization in Solids with Flip-Back of I-Spin Magnetization. *J. Magn. Reson.* **1979**, *36*, 453–457. https://doi.org/10.1016/0022-2364(79)90124-0.

(82) Lipton, A. S.; Sears, J. A.; Ellis, P. D. A General Strategy for the NMR Observation of Half-Integer Quadrupolar Nuclei in Dilute Environments. *J. Magn. Reson.* **2001**, *151*, 48–59. https://doi.org/10.1006/jmre.2001.2353.

(83) Hall, D. A.; Maus, D. C.; Gerfen, G. J.; Inati, S. J.; Becerra, L. R.; Dahlquist, F. W.; Griffin, R. G. Polarization-Enhanced NMR Spectroscopy of Biomolecules in Frozen Solution. *Science.* **1997**, *276*, 930–932. https://doi.org/10.1126/science.276.5314.930.

(84) Barnes, A. B.; De Paëpe, G.; van der Wel, P. C. A.; Hu, K.-N.; Joo, C.-G.; Bajaj, V. S.; Mak-Jurkauskas, M. L.; Sirigiri, J. R.; Herzfeld, J.; Temkin, R. J.; et al. High-Field Dynamic Nuclear Polarization for Solid and Solution Biological NMR. *Appl. Magn. Reson.* **2008**, *34*, 237–263. https://doi.org/10.1007/s00723-008-0129-1.

(85) Kobayashi, T.; Perras, F. A.; Goh, T. W.; Metz, T. L.; Huang, W.; Pruski, M. DNP-Enhanced Ultrawideline Solid-State NMR Spectroscopy: Studies of Platinum in Metal–Organic Frameworks. *J. Phys. Chem. Lett.* **2016**, *7*, 2322–2327. https://doi.org/10.1021/acs.jpclett.6b00860.

(86) Eichele, K.; Chan, J. C. C.; Wasylishen, R. E.; Britten, J. F. Single-Crystal Cobalt-59 NMR Study of Tris(2,4-Pentanedionato- O,O ‘)Cobalt(III). *J. Phys. Chem. A* **1997**, *101*, 5423–5430. https://doi.org/10.1021/jp970370i.

(87) Ooms, K. J.; Bernard, G. M.; Kadziola, A.; Kofod, P.; Wasylishen, R. E. Solid-State 13C and 59Co NMR Spectroscopy of 13C-Methylcobalt(Iii) Complexes with Amine Ligands. *Phys. Chem. Chem. Phys.* **2009**, *11*, 2690. https://doi.org/10.1039/b820753d.

(88) Medek, A.; Frydman, V.; Frydman, L. 59Co NMR Studies of Diamagnetic Porphyrin Complexes in the Solid Phase. *J. Phys. Chem. B* **1997**, *101*, 8959–8966. https://doi.org/10.1021/jp972043g.

(89) Medek, A.; Frydman, V.; Frydman, L. Central Transition Nuclear Magnetic Resonance in the Presence of Large Quadrupole Couplings: Cobalt-59 Nuclear Magnetic Resonance of Cobaltophthalocyanines. *J. Phys. Chem. A* **1999**, *103*, 4830–4835. https://doi.org/10.1021/jp990410d.

(90) Walter, T. H.; Turner, G. L.; Oldfield, E. Oxygen-17 Cross-Polarization Nmr Spectroscopy of Inorganic Solids. *J. Magn. Reson.* **1988**, *76*, 106–120. https://doi.org/10.1016/0022-2364(88)90205-3.

(91) Lo, A. Y. H.; Bitterwolf, T. E.; Macdonald, C. L. B.; Schurko, R. W. Solid-State 93 Nb

and 13 C NMR Investigations of Half-Sandwich Niobium(I) and Niobium(V) Cyclopentadienyl Complexes. *J. Phys. Chem. A* **2005**, *109*, 7073–7087. https://doi.org/10.1021/jp0521499.

For Table of Contents Only

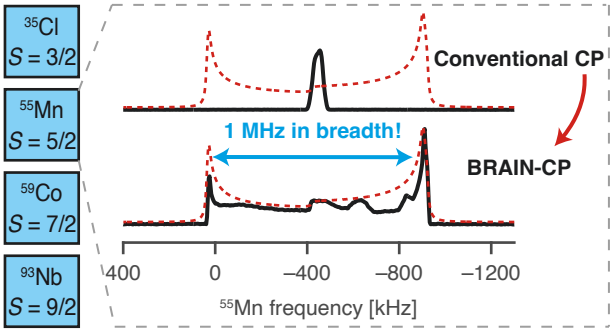

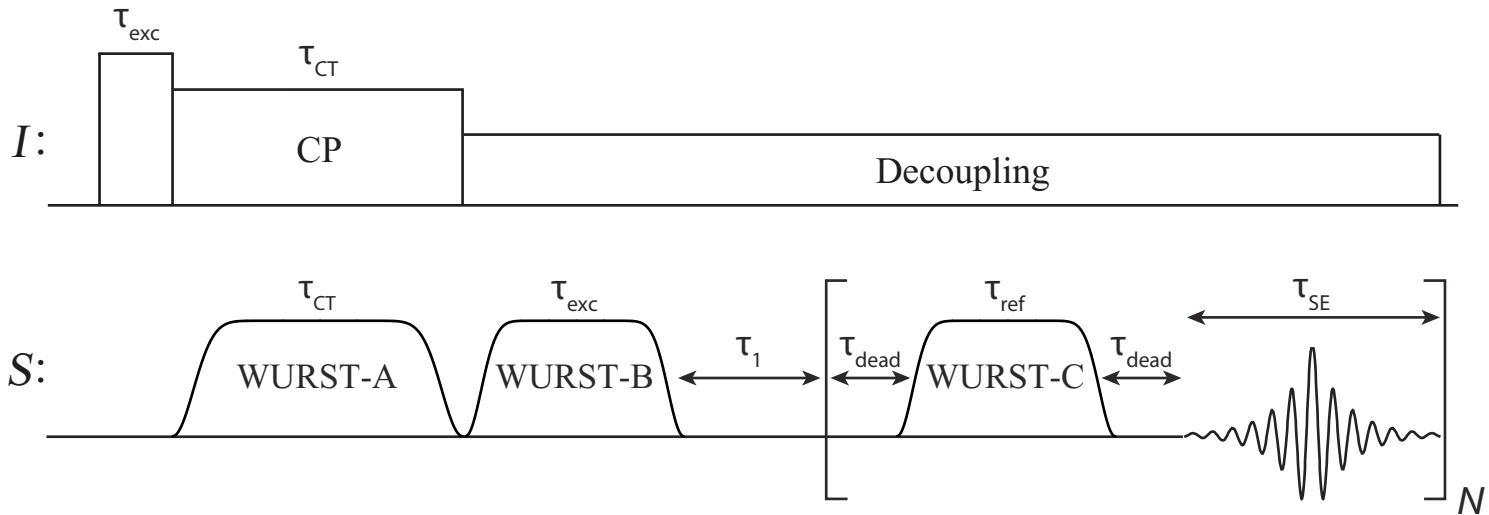

Scheme 1. Schematic representation of the BRAIN-CP pulse sequence

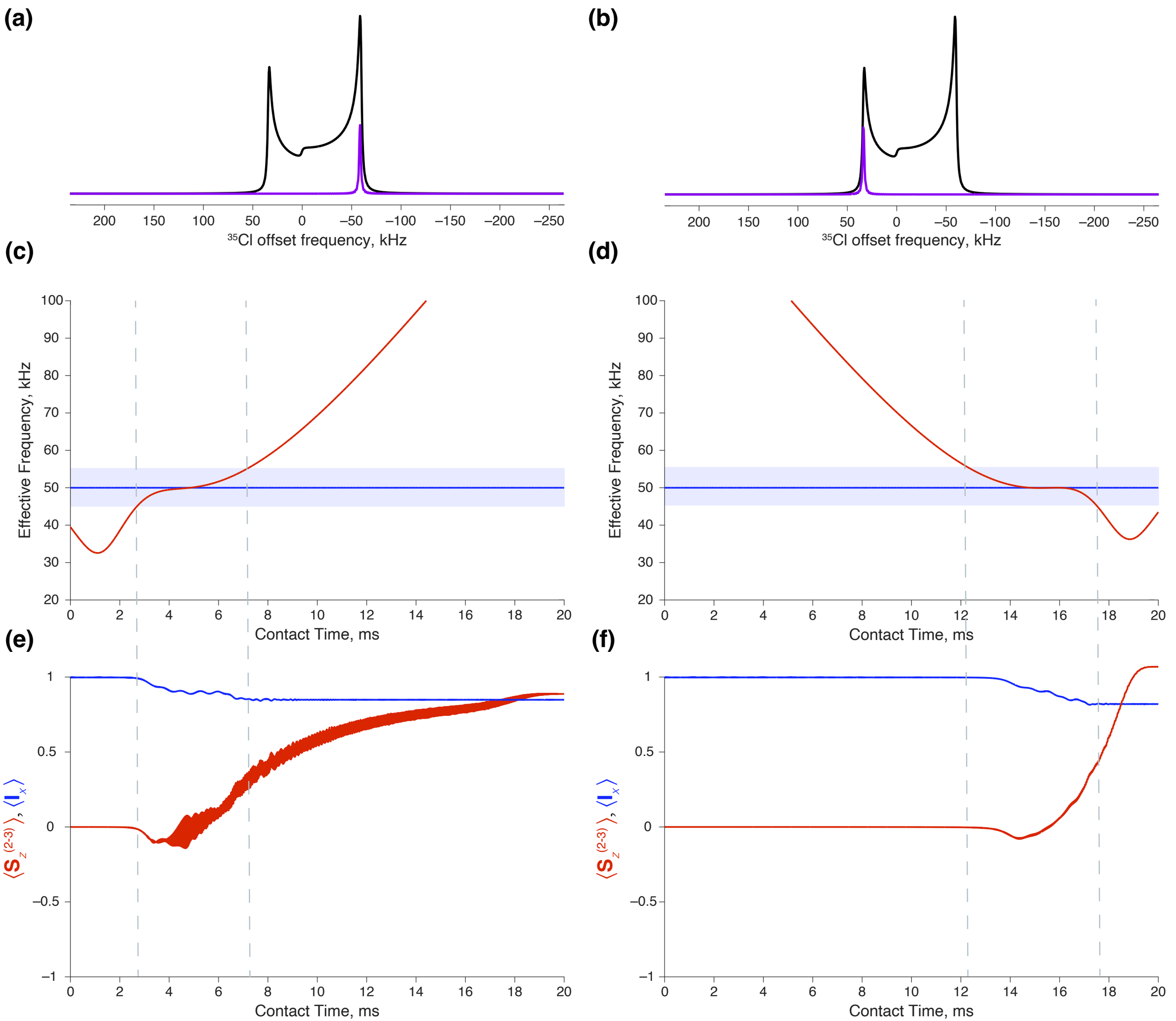

Figure 1: Ideal ^{35}Cl (S = 3/2) pattern powder patterns (C_Q = 6.5 MHz and η_Q = 0) and single crystal spectra for EFG tensor orientations of (a) β = π/4 and (b) β = π/2 (b) with respect to the external field $\mathbf{B}_0$. Analytical (c and d) and numerical (e and f) numerical simulations of $I \rightarrow S$ CP during the contact time, τ_{CT}. In every case, the initial density matrix $\rho(t_0) = \mathbf{I}_x$. The middle row (c and d) shows $\nu_{e,S}(\beta,t)$ (red line, calculated according to Equation 2) and $\nu_{1,I}$ (blue line, set to 50 kHz) plotted as a function of contact time for a BRAIN-contact pulse of τ_{CT} = 20 ms, Δ = 175 kHz, $\nu_{1,S}$ = 25 kHz, and the direction of the sweep from low to high frequency. The blue box surrounding $\nu_{1,I}$ highlights the regions between 45 and 55 kHz, representing the broadening of the matching conditions due to hetero- and homonuclear dipolar interactions. Intersections between $\nu_{e,S}(\beta,t)$ and the blue box are indicated by the dashed vertical lines, which are used to compare the HH matches in analytical and numerical simulations. The numerical simulations for a 4-spin system (3 × ^{1}H and 1 × ^{35}Cl) are shown in the bottom row (e and f). The amounts of polarization are normalized with respect to their theoretical maximum. Conditions identical to those in the analytical simulations are used. The calculations are done for an offset of $\Omega_S/2\pi$ = –15 kHz, which corresponds to the center of gravity of the powder pattern.

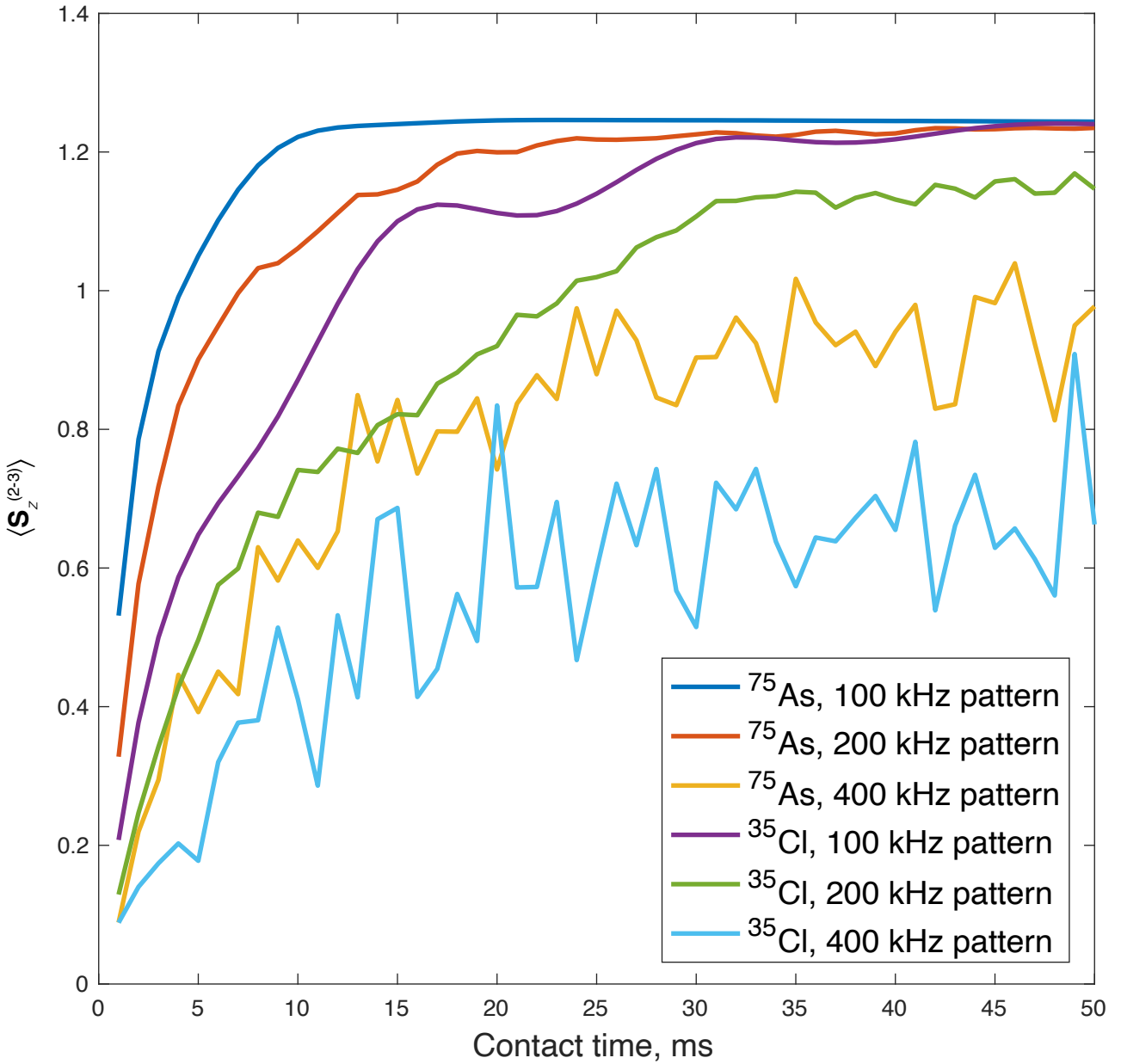

Figure 2: Numerical simulations of $\langle \mathbf{S}_z^{(2\text{-}3)} \rangle$ for an $I \rightarrow S$ CP at the end of the BRAIN contact pulse calculated as a function of increasing values of τ_{CT} for the $\beta = \pi/2$ isochromat, where values of $C_Q(^{35}Cl)$ and $C_Q(^{75}As)$ are used to generate CT pattern breadths of 100, 200, and 400 kHz. In every case, $\eta_Q = 0$, $\nu_{1,I} = 50$ kHz, Δ is set to 1.5× the pattern breadth, and $\Omega_S/2\pi$ is set to the center of gravity of the powder pattern.

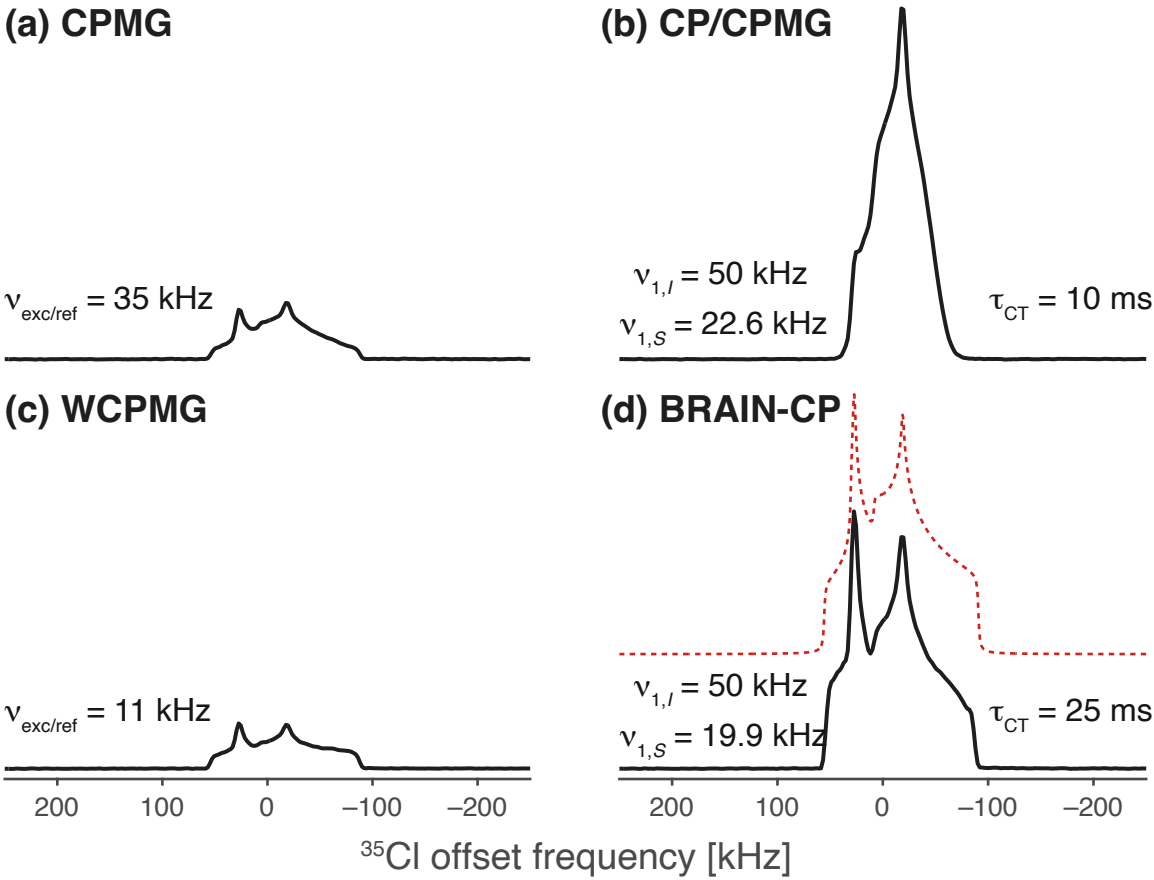

Figure 3. ^{35}Cl SSNMR spectra of glycine HCl acquired at 14.1 T with the indicated pulse sequences. The RF powers for the excitation and refocusing pulses are displayed next to each DE spectrum. Experimentally optimized HH matching conditions and contact times are shown for CP experiments. All spectra are displayed on the same relative intensity scale. The simulated ideal powder pattern is shown as the trace in red above the spectrum acquired using BRAIN-CP (d).

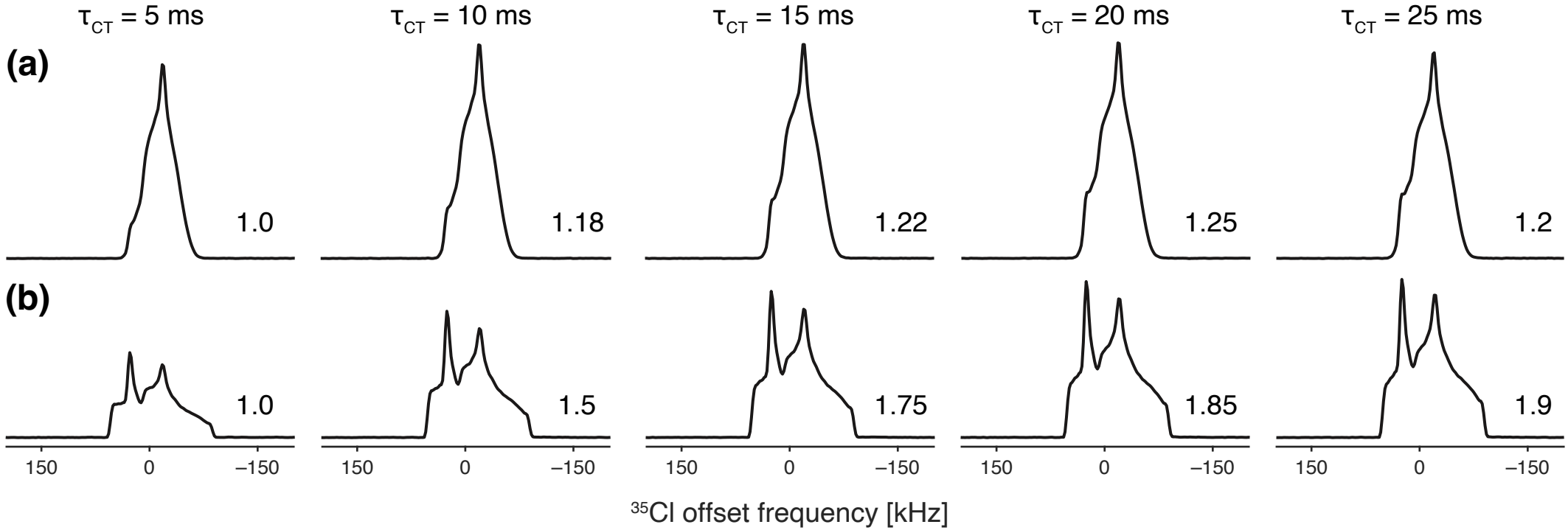

Figure 4. ^{35}Cl SSNMR spectra of glycine HCl acquired at 14.1 T using CP/CPMG (a) and BRAIN-CP (b) using contact times from 5 ms to 25 ms (left to right). The pattern areas of each spectrum are measured by integration and compared to the first spectrum of each row, which is normalized to 1.0. All spectra are presented on the same relative intensity scale.

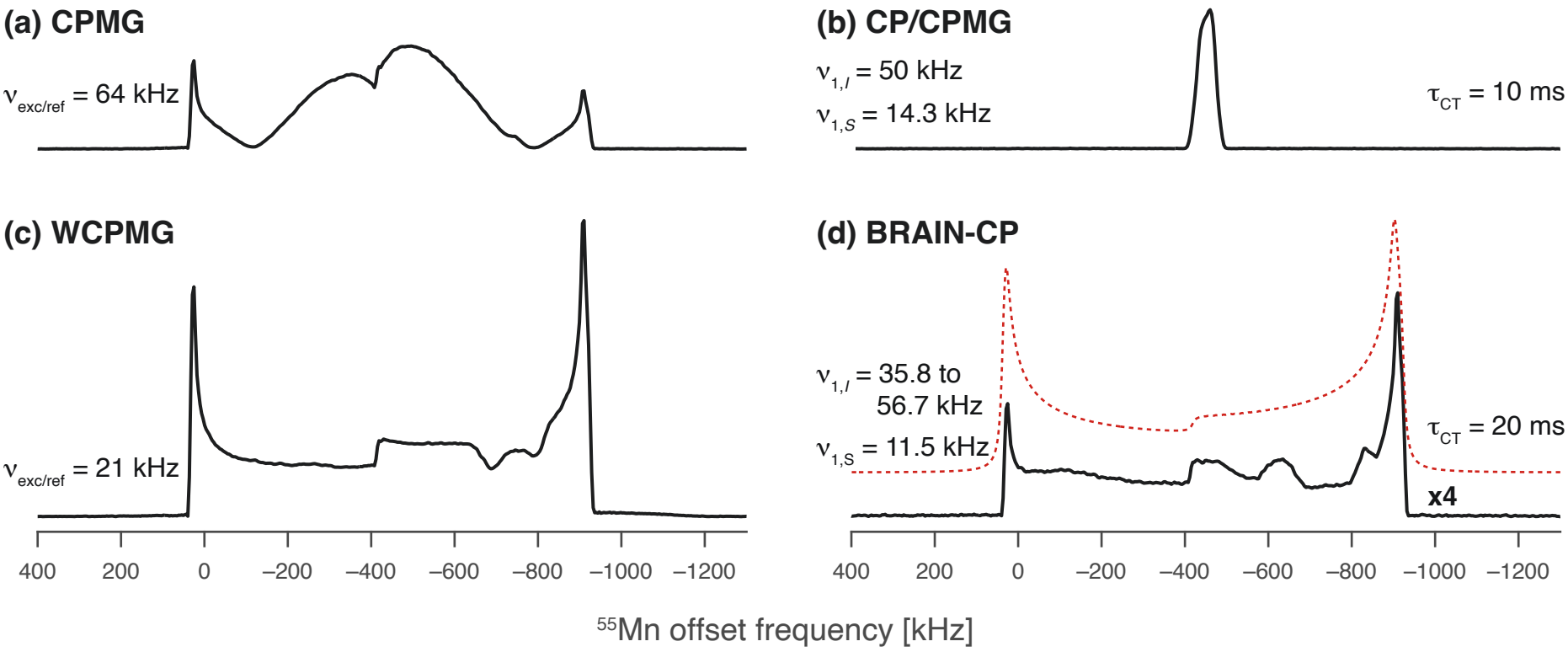

Figure 5. ^{55}Mn SSNMR spectra of η^5-$CpMn(CO)_3$ acquired at 14.1 T with the indicated pulse sequences. The RF powers for the excitation and refocusing pulses are displayed next to each DE spectrum. Experimentally optimized HH matching conditions and contact times are displayed for CP experiments.The simulated ideal powder pattern is shown as the trace in red above the spectrum acquired using BRAIN-CP (d). The intensity of (d) is scaled by a factor of 4 relative to all other spectra.

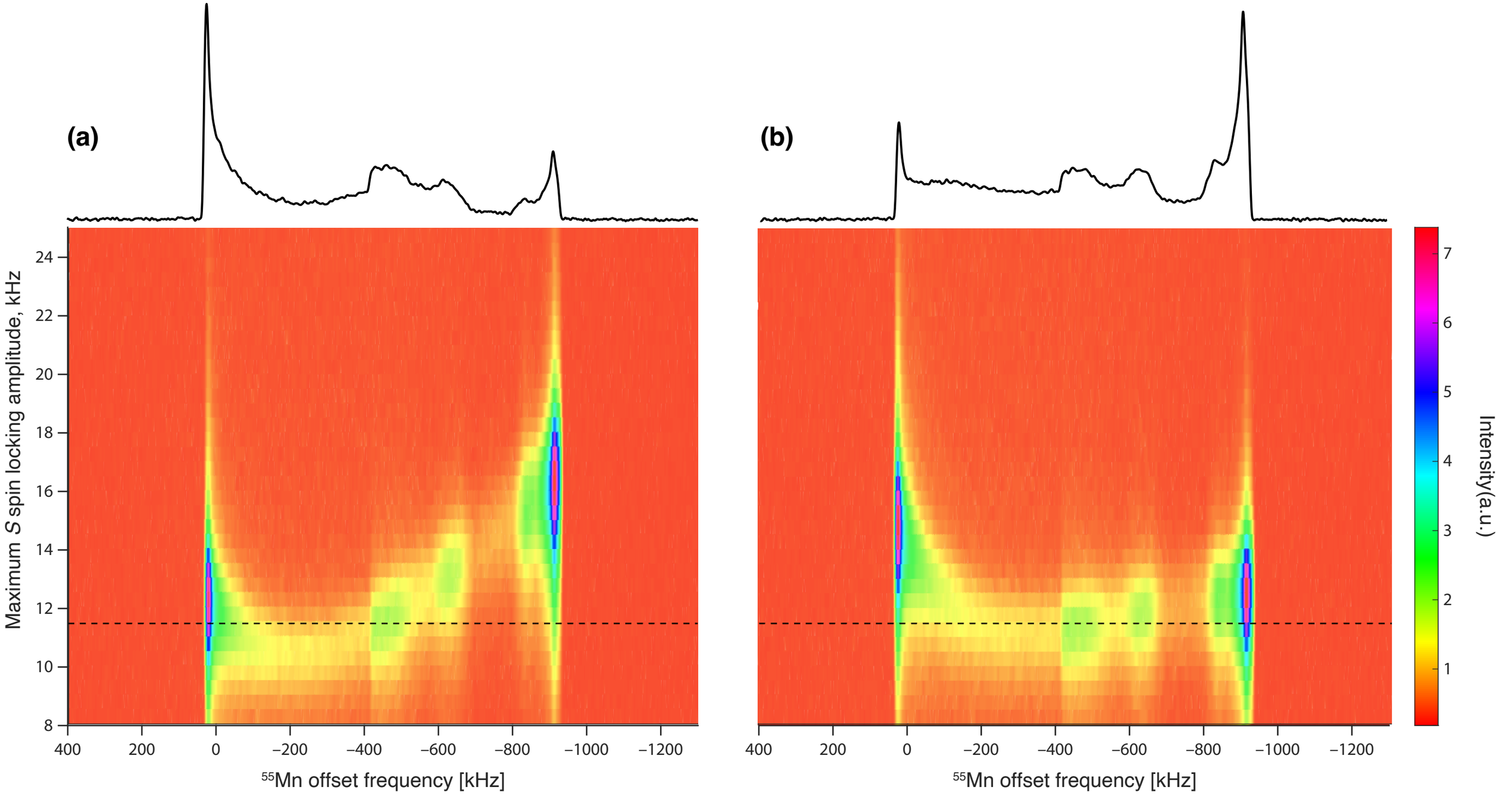

Figure 6. ^{1}H-^{55}Mn BRAIN-CP static SSNMR spectra of η^5-CpMn(CO)$_3$ acquired at 14.1 T using (a) a constant ^{1}H spin-locking pulse of 40 kHz and (b) a ramped ^{1}H spin-locking pulse from 35.8 kHz to 56.7 kHz. For each case, $\nu_{1,S}$ is arrayed using calibrated spin locking powers from 8 to 25 kHz in increments of 0.5 kHz. The dashed line at $\nu_{1,S}$ = 11.5 kHz indicates the best matching conditions that result in the most uniform powder pattern of highest intensity, which is displayed above each contour plots.

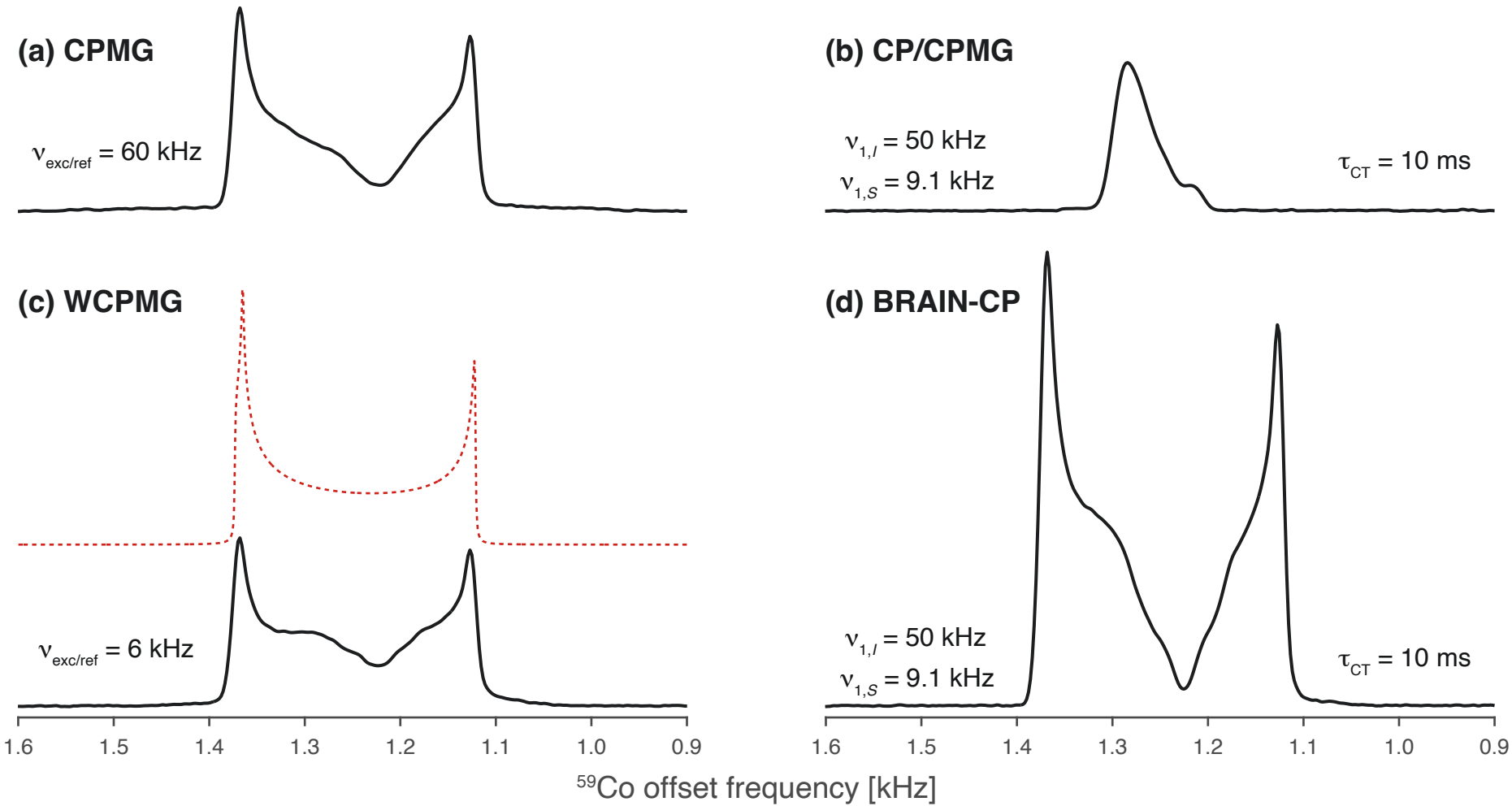

Figure 7. ^{59}Co SSNMR spectra of $[Co(NH_3)_5Cl]Cl_2$ acquired at 14.1 T with the indicated pulse sequences. The RF powers for the excitation and refocusing pulses are displayed next to each DE spectrum. Experimentally optimized HH matching conditions and contact times are displayed for CP experiments. The simulated ideal powder pattern is shown as the trace in red above the spectrum acquired using WCPMG (c). All spectra are presented on the same relative intensity scale.

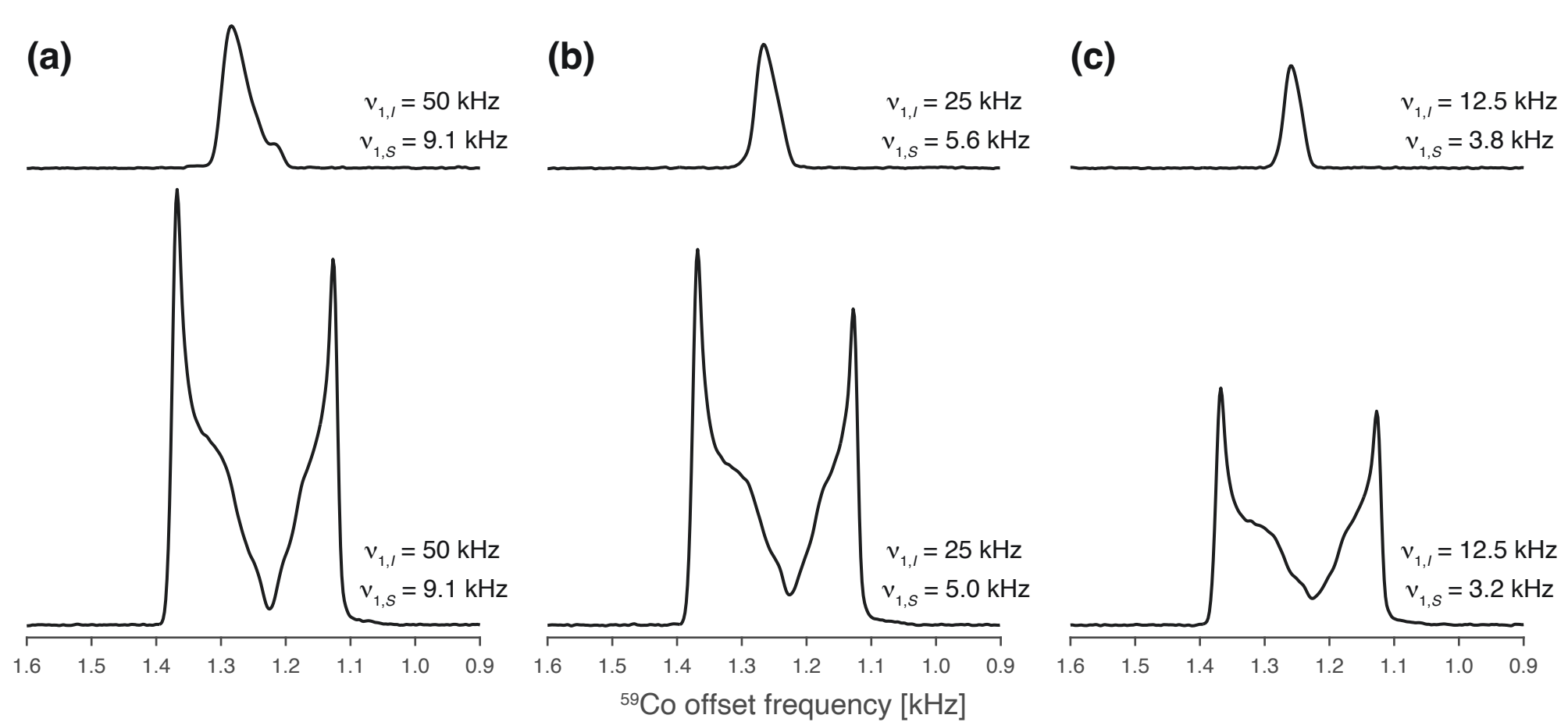

Figure 8. ^{59}Co SSNMR spectra of $[Co(NH_3)_5Cl]Cl_2$ acquired at 14.1 T with CP/CPMG (top row) and BRAIN-CP (bottom row). The proton spin locking amplitude $\nu_{1,I}$ are (a) 50 kHz, (b) 25 kHz, and (c) 12.5 kHz, with the experimentally optimized *S* HH matching powers shown for each experiment. For all experiments, τ_{CT} = 10 ms. All spectra are displayed on the same relative intensity scale.

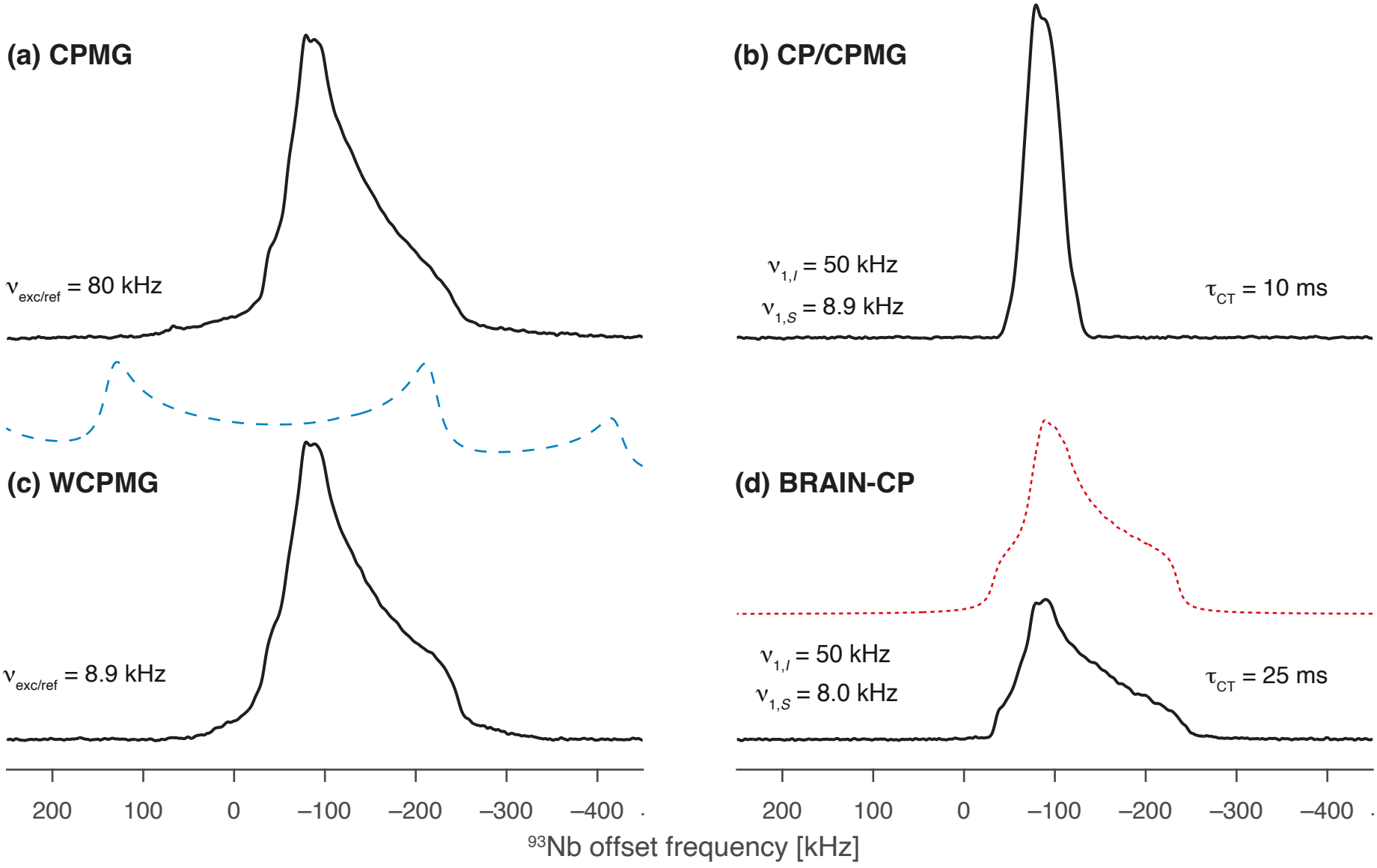

Figure 9. ^{93}Nb SSNMR spectra of $CpNbCl_4$ acquired at 14.1 T with the indicated pulse sequences. The RF powers for the excitation and refocusing pulses are displayed next to each DE spectrum. Experimentally optimized HH matching conditions and contact times are displayed for CP experiments. All spectra are plotted on the same intensity scale. The simulated ideal powder pattern of the STs appearing within the displayed spectral window is shown in blue above (c). The simulated ideal powder pattern for the CT is shown as the trace in red above the spectrum acquired using BRAIN-CP (d).

Supporting Information for

"Broadband Cross Polarization to Half-Integer Quadrupolar Nuclei: Wideline Static NMR Spectroscopy"

James J. Kimball[1,2], Adam R. Altenhof[1,2], Michael J. Jaroszewicz[3], and Robert W. Schurko[1,2]*

1. Department of Chemistry & Biochemistry, Florida State University, Tallahassee, FL 32306
2. National High Magnetic Field Laboratory, Tallahassee, FL 32310
3. Department of Chemical & Biological Physics, Weizmann Institute of Science, Rehovot, Israel 7610001

*Author to whom correspondence should be addressed.
Phone: (850)645-8614, E-mail: rschurko@fsu.edu

Supporting Information Provided:

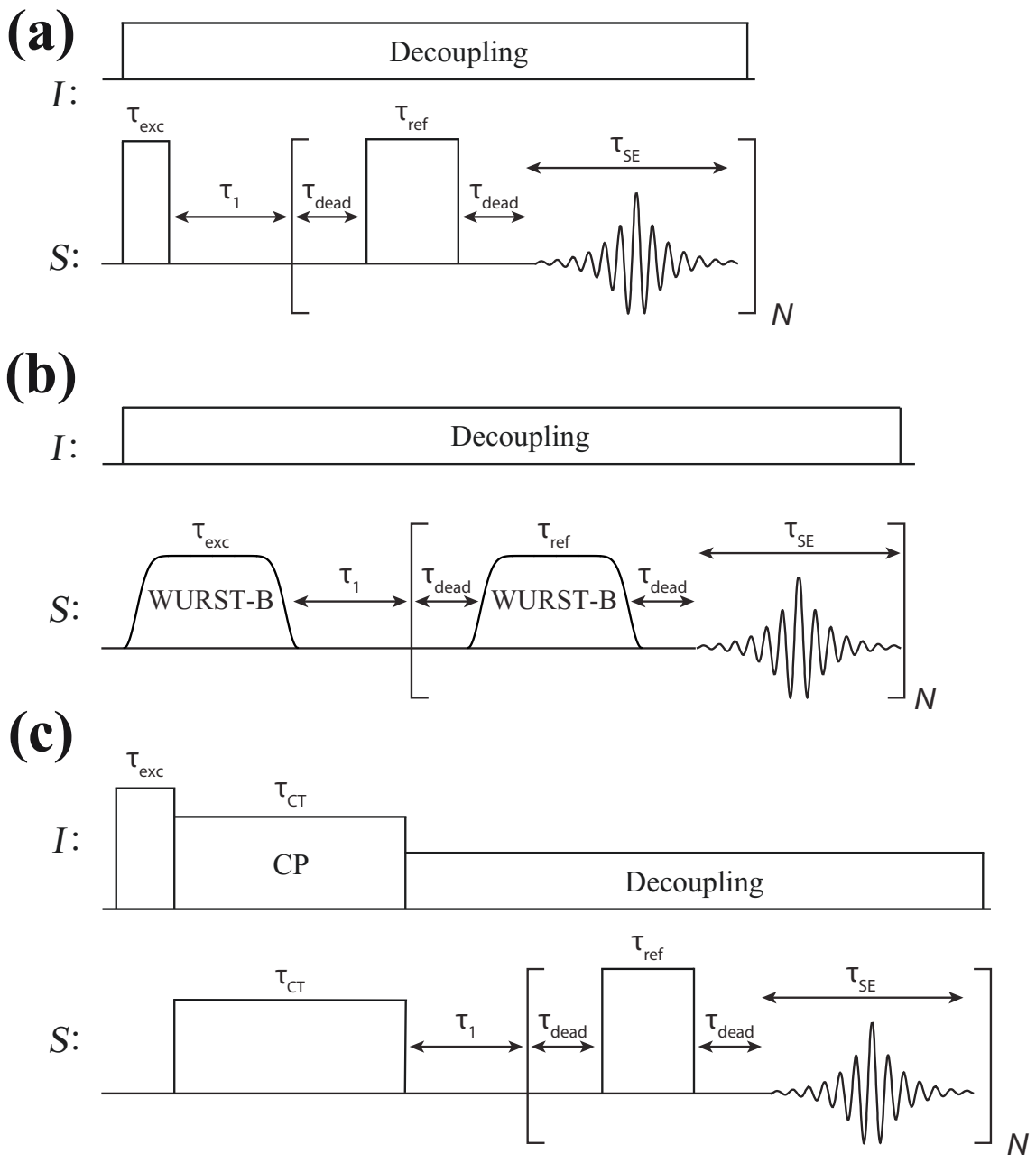

Scheme S1. Schematic representation of the (a) CPMG, (b) WCPMG, and (c) CP/CPMG pulse sequences

Table S1. Experimental Parameters for CPMG Spectra

Figure Number	3	5	7	9
Compound	Glycine HCl	η-$CpMn(CO)_3$	$[Co(NH_3)_5Cl]Cl_2$	$CpNbCl_4$
Larmor Frequency (MHz)	58.79	148.74	142.36	146.86
Number of Transients	16	256	16	128
Recycle Delay (s)	1	1	1	1
Dwell Time (μs)	1	0.534	1	1
Number of Meiboom-Gill loops, *N*	50	50	40	50
Spin Echo Length, τ_{SE} (μs)	300	200	200	250
Acquisition Time (ms)	16.7	17.7	12.4	13.9
Ring-Down Delay, τ_{dead} (μs)	10	50	50	10
Excitation Pulse Width, τ_{exc} (μs)	3.57	1.3	1.04	0.625
Refocusing Pulse Width, τ_{ref} (μs)	7.14	2.6	2.09	1.25
Excitation Pulse Power, ν_{exc} (kHz)	35	64.1	60	80
Refocusing Pulse Power, ν_{ref} (kHz)	35	64.1	60	80
^{1}H CW Decoupling RF Power (kHz)	50	50	50	50
Spectrum Width (kHz)	1000	1875	1000	1000

Table S2. Experimental Parameters for CP/CPMG Spectra

Figure Number	3	5	7	9
Compound	Glycine HCl	η-$CpMn(CO)_3$	$[Co(NH_3)_5Cl]Cl_2$	$CpNbCl_4$
Larmor Frequency (MHz)	58.79	148.74	142.36	146.86
Number of Transients	16	256	16	128
Recycle Delay (s)	2	15	20	5
Dwell Time (μs)	1	0.534	1	1
Number of Meiboom-Gill loops, *N*	50	50	40	50
Spin Echo Length, τ_{SE} (μs)	300	200	200	250
Acquisition Time (ms)	16.8	17.7	12.4	13.9
Ring-Down Delay, τ_{dead} (μs)	10	50	50	10
^{1}H Excitation Pulse Length (μs)	3.33	3.05	3	3.25
^{1}H Excitation Pulse Amplitude (kHz)	75	82	93	77
Contact Pulse Length, τ_{CT} (ms)	10	10	10	10
^{1}H Spin-lock Power, $\nu_{1,I}$ (kHz)	50	50	50	50
S Spin-lock Power, $\nu_{1,S}$ (kHz)	22.6	14.3	9.1	8.9
Refocusing Pulse Width, τ_{ref} (μs)	7.14	2.6	2.09	1.25
Refocusing Pulse Power, ν_{ref} (kHz)	35	64.1	60	80
^{1}H CW Decoupling RF Power (kHz)	50	50	50	50
Spectrum Width (kHz)	1000	1875	1000	1000

Table S3. Experimental Parameters for WCPMG Spectra

Figure Number	3	5	7	9
Compound	Glycine HCl	η-$CpMn(CO)_3$	$[Co(NH_3)_5Cl]Cl_2$	$CpNbCl_4$
Larmor Frequency (MHz)	58.79	148.74	142.36	146.86
Number of Transients	16	256	16	128
Recycle Delay (s)	1	1	1	1
Dwell Time (μs)	1	0.534	1	1
Number of Meiboom-Gill loops, *N*	50	50	40	50
Spin Echo Length, τ_{SE} (μs)	300	200	200	250
Acquisition Time (ms)	18.9	17.7	14.2	16.4
Ring-Down Delay, τ_{dead} (μs)	10	50	50	10
WURST-B length, τ_B (μs)	50	50	50	50
WURST-B Sweep width, $\Delta\nu_B$ (kHz)	300	1750	500	450
WURST-B Amplitude, $\nu_{1,B}$ (kHz)	10.9	20.8	5.75	5
WURST-C length, τ_C (μs)	50	50	50	50
WURST-C Sweep width, $\Delta\nu_C$ (kHz)	300	1750	500	450
WURST-C Amplitude, $\nu_{1,C}$ (kHz)	10.9	20.8	5.75	5
^{1}H CW Decoupling RF Power (kHz)	50	50	50	50
Spectrum Width (kHz)	1000	1875	1000	1000

Table S4. Experimental Parameters for BRAIN-CP Spectra

Figure Number	3	5	7	9
Compound	Glycine HCl	η-$CpMn(CO)_3$	$[Co(NH_3)_5Cl]Cl_2$	$CpNbCl_4$
Larmor Frequency (MHz)	58.79	148.74	142.36	146.86
Number of Transients	16	256	16	128
Recycle Delay (s)	2	10	20	5
Dwell Time (μs)	1	0.534	1	1
Number of Meiboom-Gill loops, *N*	50	50	40	50
Spin Echo Length, τ_{SE} (μs)	300	200	200	250
Acquisition Time (ms)	18.9	17.1	14.2	16.4
Ring-Down Delay, τ_{dead} (μs)	10	50	50	10
^{1}H Excitation Pulse Length (μs)	3.33	2.88	3	3.25
^{1}H Excitation Pulse Amplitude (kHz)	75	87	93	77
^{1}H Spin-lock Power, $\nu_{1,I}$ (kHz)	50	35.8 to 56.7	50	50
Contact Pulse Length, τ_{CT} (ms)	20	20	10	25
WURST-A Sweep width, $\Delta\nu_A$ (kHz)	300	1750	500	450
WURST-A Amplitude, $\nu_{1,A}$ (kHz)	19.9	11.5	9.1	8
WURST-B length, τ_B (μs)	50	50	50	50
WURST-B Sweep width, $\Delta\nu_B$ (kHz)	300	1750	500	450
WURST-B Amplitude, $\nu_{1,B}$ (kHz)	10.9	20.8	5.75	5
WURST-C length, τ_C (μs)	50	50	50	50
WURST-C Sweep width, $\Delta\nu_C$ (kHz)	300	1750	500	450
WURST-C Amplitude, $\nu_{1,C}$ (kHz)	10.9	20.8	5.75	5
^{1}H CW Decoupling RF Power (kHz)	50	50	50	50
Spectrum Width (kHz)	1000	1875	1000	1000

Supplement 1: On the use of CPMG for RF power calibrations

In this section, it is demonstrated how the CPMG sequence can be used for facile and accurate calibrations of RF amplitudes. This avoids the necessity of calibrating RF powers on a separate standard having a spectrum with a sharp peak (*i.e.*, solution or solids), which may or may not be available. The basic idea is that the transmitter is set near a clearly identifiable discontinuity of a powder pattern in a spectrum of high S/N and the excitation pulse width (τ_{exc}) is arrayed (from low to high values) using a constant RF power and refocusing pulse length (τ_{ref}). The value of τ_{exc} resulting in the highest signal at the transmitter frequency is interpreted as that corresponding to a 90° tip angle.

Figure S1 shows four sets of spectra acquired as a function of excitation pulse length for 0.1M NaCl in D_2O (**Fig. S1a**), solid NaCl (**Fig. S1b**), and glycine HCl (**Figs. S1c** and **S1d**), with the RF power set to 50 W in every case. The first two sets of data are acquired with a Bloch decay sequence, whereas the second two sets are acquired using CPMG. We note that the first two sets of spectra (**Figs. S1a** and **S1b**) are phased (*i.e.*, 0^{th} + 1^{st} order phasing), whereas the latter two data sets (**Figs. S1c** and **S1d**) are processed via magnitude correction (*i.e.*, no phasing). For the Bloch decay experiments, the pulse width resulting in a null signal is interpreted as that corresponding to a 180° flip angle, which is 21 μs in both **Figs. S1a** and **S1b**, as indicated by the red arrow. Altenhof *et al*. recently demonstrated that homonuclear dipolar interactions can influence the lineshape of wideline powder patterns acquired in conventional 90°-180° CPMG-type sequences.[1] As such, we avoid using the refocusing pulse width for power calibrations involving wideline or UW patterns; rather, the refocusing pulse is held constant and the excitation pulse width is arrayed, and the pulse width giving maximum signal is interpreted as that corresponding to a 90° flip angle. This is demonstrated in **Figs. S1c** and **S1d**, where two different values of τ_{ref} (6 μs and 8 μs, respectively)

are used. While the length of τ_{ref} does have an effect on which excitation pulse results in null signal, the value of τ_{exc} giving maximum signal (5 μs, indicated by the red arrow above the array in **Fig. S1c**) is the same in both cases. Since excitation of a SOQI-dominated CT pattern is involved, this pulse width is the selective π/2 pulse width, τ_{exc}(sel) = 5 μs, which for a spin-3/2 nucleus corresponds to a non-selective pulse width τ_{exc}(non-sel) = 10 μs, which is in agreement with the calibrated 90° pulse widths of 10.5 μs obtained from the standard calibration curves in **Figs. S1a**

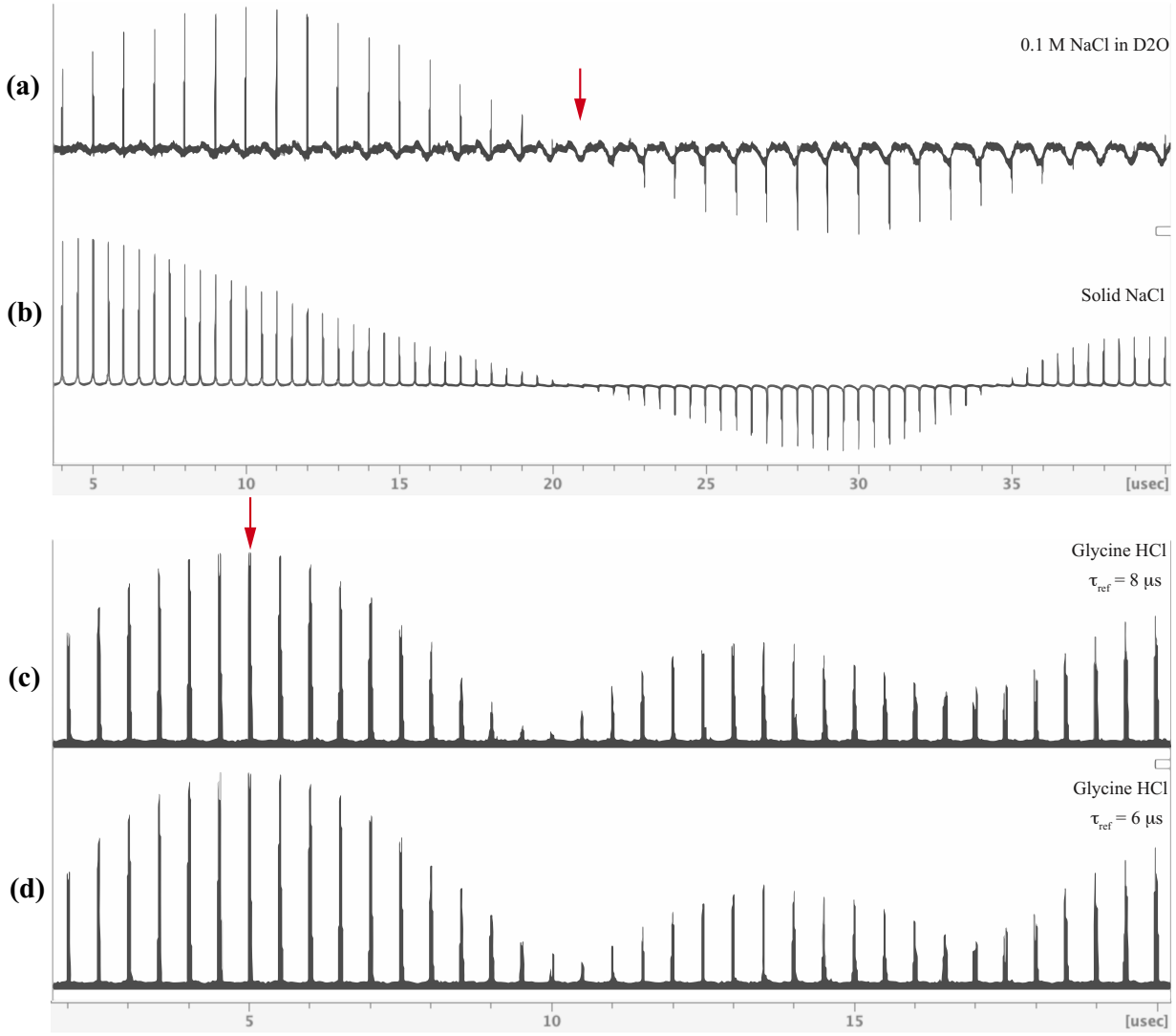

Figure S1: ^{35}Cl spectra of (a) 0.1M NaCl in D_2O, (b) solid NaCl, and (c and d) glycine HCl acquired using a Bloch decay (a and b) and CPMG (c and d) as a function of excitation pulse length. The RF power is set to 50 W in every case, and the refocusing pulse width is set to 8 μs and 6 μs in (c) and (d), respectively. The red arrows indicate the excitation pulse widths which are used for power calibrations (see text for more detail).

and **S1b**. It is noted that care must be given to only interpret the signal appearing at the transmitter frequency, as offset effects could result in inaccurate power calibrations.

Supplement 2: Derivation of the HH matching conditions for BRAIN-CP to HIQN

The Hamiltonian for a FS pulse with a time-dependent amplitude and phase in the rotating frame is given by[2]

$$\mathbf{H}_S = \Omega_S \mathbf{S}_z + \omega_{1,S} \cdot A(t)[\mathbf{S}_x \cos\psi(t) + \mathbf{S}_y \sin\psi(t)] \quad (1)$$

where $\Omega_S = \omega_0^S - \omega_{\mathrm{RF}}^S$ is the transmitter offset (ω_0^S is the resonance frequency in the laboratory frame and ω_{RF}^S is the transmitter frequency), $\omega_{1,S} = 2\pi\nu_{1,S} = -\gamma_S B_{1,S}$ is the maximum amplitude of the pulse applied to the *S* spins, and $\mathbf{S}_x$, $\mathbf{S}_y$, and $\mathbf{S}_z$ are the spin-angular momentum operators. For a WURST pulse, the amplitude modulation of the RF is described as $A(t) = \left[1 - |\cos\pi t/\tau_{\mathrm{p}}|^N\right]$, where N is an integer. The phase profile $\psi(t)$ is quadratic in form and corresponds to a linear frequency sweep

$$\psi(t) = \pm\left[-\frac{\Delta}{2\tau_{\mathrm{p}}} t^2 + \left(\omega_{\mathrm{off}} + \frac{\Delta}{2}\right) t\right] \quad (2)$$

where ω_{off}, Δ, and τ_{p} are an arbitrary initial offset, the range of the frequency sweep, and the duration of the WURST pulse, respectively. The direction of the frequency sweep is from high-to-low (HtoL) frequency or low-to-high (LtoH) frequency when Equation (2) is multiplied by +1 or –1, respectively.[3] The Hamiltonian in Equation (1) can be transformed to a frequency modulated (FM) frame[4] that rotates synchronously with $\psi(t)$ (denoted as $\mathbf{H}'$), in order to better monitor the trajectory of the spin polarization during irradiation with a WURST pulse:

$$\mathbf{H}_S'(t) = [\Omega_S - \omega_{\mathrm{p}}(t)]\mathbf{S}_z + \omega_{1,S} A(t) \mathbf{S}_x \quad (3)$$

where the instantaneous frequency $\omega_{\mathrm{p}}(t) = d\psi(t)/dt = \pm[-(\Delta/\tau_p)t + \Delta/2]$. If a $S = 3/2$ nucleus (*e.g.*, ^{35}Cl) is being irradiated by the pulse, the FM Hamiltonian can be expressed in the basis of the fictitious spin-1/2 operators[5] (denoted as $\widetilde{\mathbf{H}}$) as

$$\begin{gathered}\widetilde{\mathbf{H}}'_S(t,\beta) = \Omega_S^{\mathrm{eff}}(t)[3\mathbf{S}_z^{1-4} + \mathbf{S}_z^{2-3}] + \omega_{1,S}A(t)\left[\sqrt{3}(\mathbf{S}_x^{1-2} + \mathbf{S}_x^{3-4}) + 2\mathbf{S}_x^{2-3}\right] \\ \omega_{\mathrm{Q}}(\beta)[\mathbf{S}_z^{1-2} + \mathbf{S}_z^{3-4}] + \omega_{\mathrm{Q},2}^{(2-3)}(\beta)\mathbf{S}_z^{2-3} + \omega_{\mathrm{Q},2}^{(1-4)}(\beta)\mathbf{S}_z^{1-4}\end{gathered} \tag{4}$$

where $\Omega_S^{\mathrm{eff}}(t) = \Omega_S - \omega_{\mathrm{p}}(t)$. Assuming an axially symmetric EFG tensor ($i.e.$, $\eta_{\mathrm{Q}} = 0$), the first- and second-order quadrupolar frequencies[6] (the latter is separated into the (2-3) and (1-4) subspaces, respectively) are

$$\begin{aligned}\omega_{\mathrm{Q}}(\beta) &= \frac{\chi_{\mathrm{Q}}}{4}(1 - 3\cos^2\beta) \\ \omega_{\mathrm{Q},2}^{(2-3)}(\beta) &= -\frac{\chi_{\mathrm{Q}}^2}{64\omega_0}(1 - \cos^2\beta)(1 - 9\cos^2\beta) \\ \omega_{\mathrm{Q},2}^{(1-4)}(\beta) &= -\frac{\chi_{\mathrm{Q}}^2}{64\omega_0}(1 - \cos^2\beta)(1 + 7\cos^2\beta)\end{aligned}$$

where $\chi_{\mathrm{Q}} = 2\pi \bullet C_{\mathrm{Q}} = e^2qQ/\hbar$ in rad s^{-1} and β is the angle between the largest component of the EFG tensor (V_{33}) and $\mathbf{B}_0$. Vega has shown that so long as $\omega_{\mathrm{Q}} \gg \omega_{1,S}$, the Hamiltonian can be separated into three commuting parts which are defined by the (1-4), (2-3), and [(1-2)-(3-4)] operators. As we are interested in only the (2-3) subspace ($i.e.$, the CT), we can re-write Equation (4), keeping only the relevant operators, as

$$\widetilde{\mathbf{H}}_S'^{(2-3)}(t,\beta) = \left[\Omega_S^{\mathrm{eff}} + \omega_{\mathrm{Q},2}^{(1)}(\beta)\right]\mathbf{S}_z^{2-3} + 2\omega_{1,S}A(t)\mathbf{S}_x^{2-3} \tag{5}$$

The effective frequency for the central transition is then given by

$$\omega_{\mathrm{e},S}^{(2-3)}(t,\beta) = \sqrt{\left[\Omega_S^{\mathrm{eff}} + \omega_{\mathrm{Q},2}^{(1)}(\beta)\right]^2 + [2\omega_{1,S}A(t)]^2} \tag{6}$$

The Hamiltonian describing the CP dynamics for an isolated spin pair ($I = 1/2 \rightarrow S = 3/2$) in which the S spin is subjected to a FS pulse in the FM frame (again using the fictitious spin-1/2 basis, keeping only elements of the (2-3) subspace), is

$$\mathbf{H}'^{(2-3)}(t,\beta) = \omega_{1I}\mathbf{I}_x + \left[\Omega_S^{\text{eff}}(t) + \omega_{\text{Q},2}^{(1)}(\beta)\right]\mathbf{S}_z^{2-3} + 2\omega_{1,S}A(t)\mathbf{S}_x^{2-3} + 2bI_z\mathbf{S}_z^{2-3} \tag{7}$$

where $\omega_{1,I} = 2\pi\nu_{1,I} = -\gamma_S B_{1,I}$ is the irradiation applied to the I spins (off-resonance effects are ignored for simplicity), and the S-spin Hamiltonian is given as in Equation (5). Any homonuclear dipolar couplings are ignored, and an $I - S$ heteronuclear dipolar coupling is considered via transformation into the EFG tensor frame of the S nucleus: DIP $\overset{(0^\circ,\theta,\psi)}{\rightarrow}$ EFG $\overset{(\alpha,\beta,0^\circ)}{\rightarrow}$ LAB, where

$$\begin{aligned} b = \; & \frac{\omega_{IS}^{\text{D}}}{8}[(3\cos^2\beta - 1)(3\cos^2\theta - 1) - 3\sin(2\beta)\sin(2\alpha)\cos(\alpha + \psi) \\ & + 3\sin^2\beta\sin^2\theta\cos(2\alpha + 2\psi)] \end{aligned}$$

where

$$\omega_{IS}^{\text{D}} = -\frac{\mu_0}{4\pi}\frac{\gamma_I\gamma_S\hbar}{r_{IS}^3}$$

The angles $(0^\circ, \theta, \psi)$ describe the orientation of the $I - S$ dipolar vector with respect to the principal axis system (PAS) of the EFG tensor.

The Hamiltonian in Equation (7) can be transformed to the doubly tilted frame[7,8] (denoted as $\mathbf{H}''$) in which all RF fields lie parallel to the z'' axis and becomes

$$\begin{aligned} \mathbf{H}''^{(2-3)}(t,\beta) = \; & \omega_{\text{e},I}\mathbf{I}_z + \omega_{\text{e},S}(t,\beta)\mathbf{S}_z^{2-3} + 4\sin\theta_I\sin\theta_S(t,\beta)b\mathbf{I}_x\mathbf{S}_x^{2-3} \\ & + 4\cos\theta_I\cos\theta_S(t,\beta)\mathbf{I}_z\mathbf{S}_z^{2-3} - 4\cos\theta_I\sin\theta_S(t,\beta)b\mathbf{I}_z\mathbf{S}_z^{2-3} \\ & - 4\sin\theta_I\cos\theta_S(t,\beta)b\mathbf{I}_x\mathbf{S}_z^{2-3} \end{aligned} \tag{8}$$

where the effective frequencies along the tilted z'' axes are

$$\omega_{\mathrm{e},I} \approx \omega_{1,I}$$
$$\omega_{\mathrm{e},S}(t,\beta) = \sqrt{\left[\Omega_S^{\mathrm{eff}}(t) + \omega_{\mathrm{Q},2}^{(1)}(\beta)\right]^2 + [2\omega_{1,S}A(t)]^2} \quad (9)$$

and the tilt angles that related the z'' axis to the z' axis in the FM frame given by

$$\cos\theta_I = \Omega_I/\omega_{\mathrm{e},I} = 0$$
$$\sin\theta_I = \omega_{1I}/\omega_{\mathrm{e},I} = 1$$
$$\cos\theta_S(t,\beta) = \left(\Omega_S^{\mathrm{eff}}(t) + \omega_{\mathrm{Q},2}^{(1)}(\beta)\right)/\omega_{\mathrm{e},S}(t,\beta)$$
$$\sin\theta_S(t,\beta) = 2\omega_{1,S}/\omega_{\mathrm{e},S}(t,\beta)$$

Using these definitions and keeping only the terms relevant to the CP process,[9,10] the Hamiltonian in Equation (8) can be re-written as

$$\mathbf{H}''^{(2-3)}(t) = \omega_{1,I}\mathbf{I}_z + \omega_{\mathrm{e},S}(t)\mathbf{S}_z^{2-3} - 4\sin\theta_S(t)b\mathbf{I}_x\mathbf{S}_z^{2-3} \quad (9)$$

Under static conditions, only the zero-quantum matching conditions are realizable and thus the time-dependent HH matching condition for spin-3/2 BRAIN-CP is

$$\omega_{1,I} = \sqrt{\left[\Omega_S^{\mathrm{eff}} + \omega_{\mathrm{Q},2}^{(1)}(\beta)\right]^2 + [2\omega_{1,S}A(t)]^2} \quad (10)$$

Equation (10) can be generalized for spin-n/2 BRAIN-CP as

$$\omega_{1,I} = \sqrt{\left[\Omega_S^{\mathrm{eff}} + \omega_{\mathrm{Q},2}^{(1)}(\beta)\right]^2 + [(n/2 + 1/2)\omega_{1,S}A(t)]^2} \quad (11)$$

Supplement 3: Polarization transfer between CT and STs

Certain isochromats of HIQN corresponding to unique orientations of an axially symmetric EFG tensor with respect to $\mathbf{B}_0$ (as defined by β, the angle between the direction of V_{33} and $\mathbf{B}_0$) have similar or identical single-quantum (SQ) transition frequencies between all Zeeman states (*i.e.*, for some angle β, the values of the orientation-dependent quadrupolar frequencies, $\omega_Q(\beta)$ arising from the central transition (CT) and satellite transitions (ST) are the same). If the transmitter is placed at or near these frequencies, these isochromats are simultaneously irradiated and the Zeeman populations of states involved in the CT can be transferred to those involved in the STs, and vice versa. In such cases, CT powder patterns display 'dips' (*i.e.*, deviations from the ideal lineshape) at the resonance frequencies of these isochromats. Previously, Altenhof *et al.* and Hansen *et al.* demonstrated this for systems of HIQN with axially symmetric EFG tensors.[11,12] In a frame rotating at $\omega_0 + \omega_Q^{(1)}(\beta) + \omega_Q^{(2)}(\beta)$ (see main text for definitions of first- and second-order quadrupolar frequencies; herein, we refer to this frame as the rotating quadrupolar frame, RQF), all Zeeman states for isochromats oriented at (or near) β = 54.74° are degenerate (or nearly degenerate). This is demonstrated in **Figure S2a** where the differences in in frequency between the $+|3/2\rangle \leftrightarrow +|1/2\rangle$ and $+|1/2\rangle \leftrightarrow -|1/2\rangle$ transitions for a spin-3/2 nucleus ($C_Q = 6.5$ MHz and $\eta_Q = 0$) are plotted as a function of the angles α and β (which describe the orientation of the EFG tensor relative to $\mathbf{B}_0$). The regions where the differences in the two sets of transitions is ≤ 1 kHz are denoted by the thick black lines, denoting the angles which correspond to isochromats with degenerate (or nearly degenerate) Zeeman states. **Figure S2b** shows a CT powder pattern for this nucleus simulated using a Hahn echo (solid blue line) compared to the ideal powder pattern (dotted red line). Departure from the ideal lineshape is clearly visible near –50 kHz, which is the region in which the resonance frequencies of

isochromats with degenerate Zeeman levels in the RQF lie. As an example, the ideal single crystal spectrum for the β = 53.3° isochromat, which corresponds to the orientation highlighted by the black line at 2.2 rad in **Fig. S2a**, is plotted in black beneath the powder patterns. As a result of the degenerate Zeeman levels, the efficiency of selective excitation and refocusing of the CT of these isochromats (and those isochromats oriented at β = 54.7°) is diminished relative to other isochromats, as demonstrated by the dip in the powder pattern.

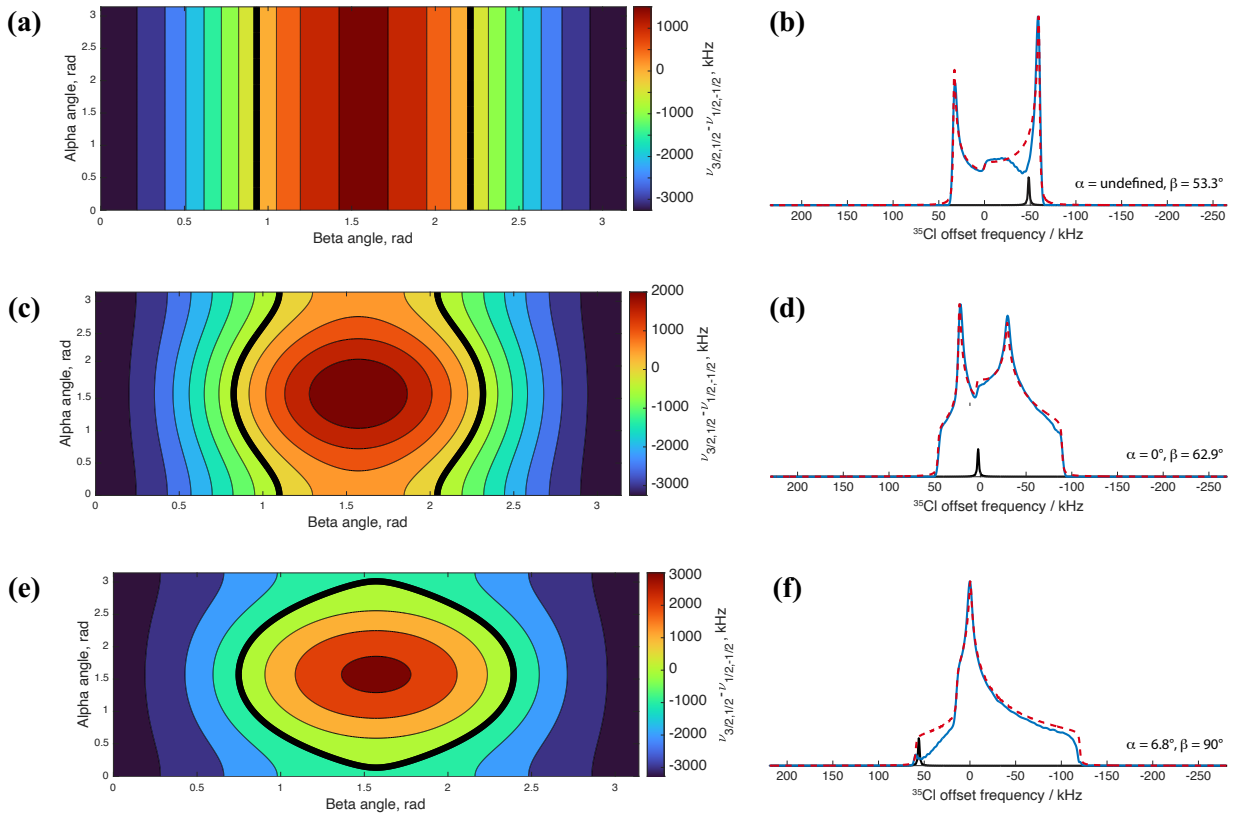

Figure S2: Contour plots showing the differences in frequency between the $+|3/2\rangle \leftrightarrow +|1/2\rangle$ and $+|1/2\rangle \leftrightarrow -|1/2\rangle$ transitions for a spin-3/2 nucleus with C_Q = 6.5 MHz and η_Q = 0 (a), 0.5 (b), and 1 (c). The regions where the difference between the two sets of transitions is ≤ 1 kHz are denoted by the thick black lines. For each value of η_Q, simulated ideal powder patterns (dotted red lines) are compared to those simulated using a Hahn echo (solid blue lines). Single crystal spectra for isochromat orientations as indicated to the right of each spectra are shown in black.

Similar results are obtained for systems of non-axially symmetric EFG tensors. In **Figs. S2c** and **S2e**, the differences in transition frequencies between the $+|3/2\rangle \leftrightarrow +|1/2\rangle$ and $+|1/2\rangle \leftrightarrow -|1/2\rangle$ transitions for a spin-3/2 nucleus ($C_Q = 6.5$ MHz and η_Q = 0.5 and 1, respectively) are plotted as a function of the angles α and β. Again, the thick black lines denote isochromat orientations for which this difference is < 1 kHz. Ideal simulated powder patterns (dotted red lines) for η_Q values of 0.5 and 1 are shown in **Figs. S2d** and **S2f**, respectively. Powder patterns simulated using a Hahn echo are shown in blue, with regions of clear departure from the ideal lineshape present in both cases. Examples of ideal single crystal spectra of isochromats with degenerate Zeeman levels (the orientations are indicated to the right) obtained from the plots in **S2c** and **S2e** is shown for both cases (black spectra). The resonance frequencies of both isochromats appear in regions where deviations between the ideal and Hahn-echo spectra are observed.

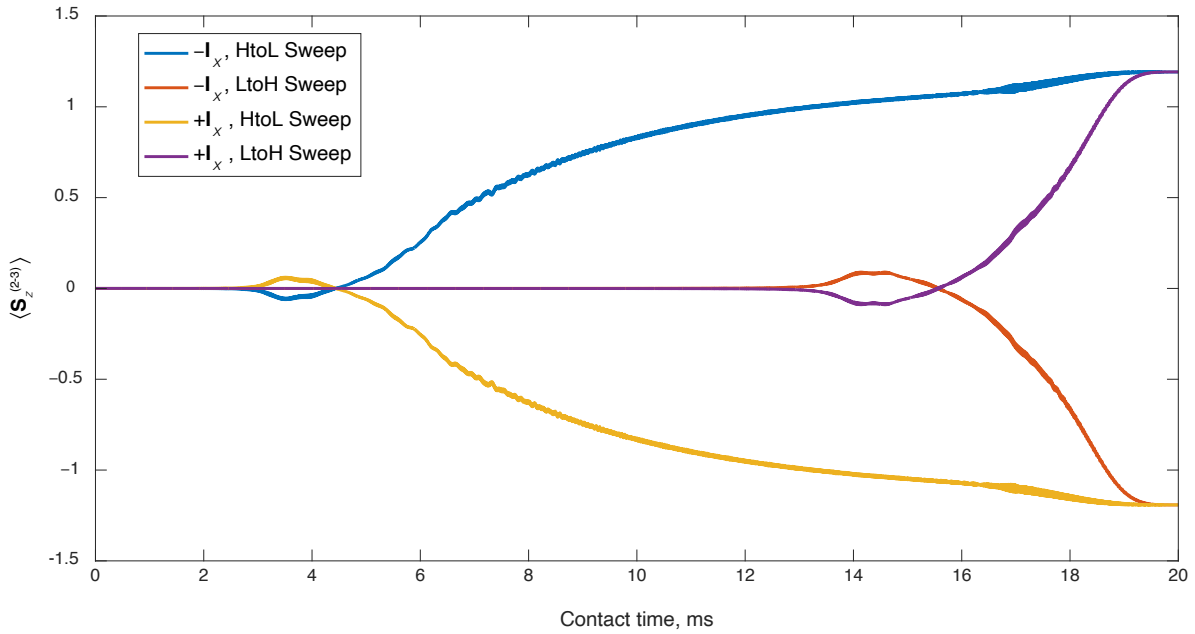

Figure S3: Numerical simulations of $\langle \mathbf{S}_z^{(2\text{-}3)} \rangle$ for the $\beta = \pi/2$ isochromat calculated using initial states of $\rho(t_0) = -\mathbf{I}_x$ (blue and orange lines) and $\rho(t_0) = +\mathbf{I}_x$ (yellow and purple lines) and WURST sweep directions of high-to-low (HtoL, blue and yellow lines) and low-to-high (LtoH, orange and purple lines). These simulations demonstrate it is possible to store the spin polarization arising from broadband CP along either the $+z$ or $-z$ axes. In every case, $C_Q = 6.5$ MHz, $\eta_Q = 0$, $\nu_{1,I} = 50$ kHz, and $\Omega_S/2\pi = -15$ kHz.

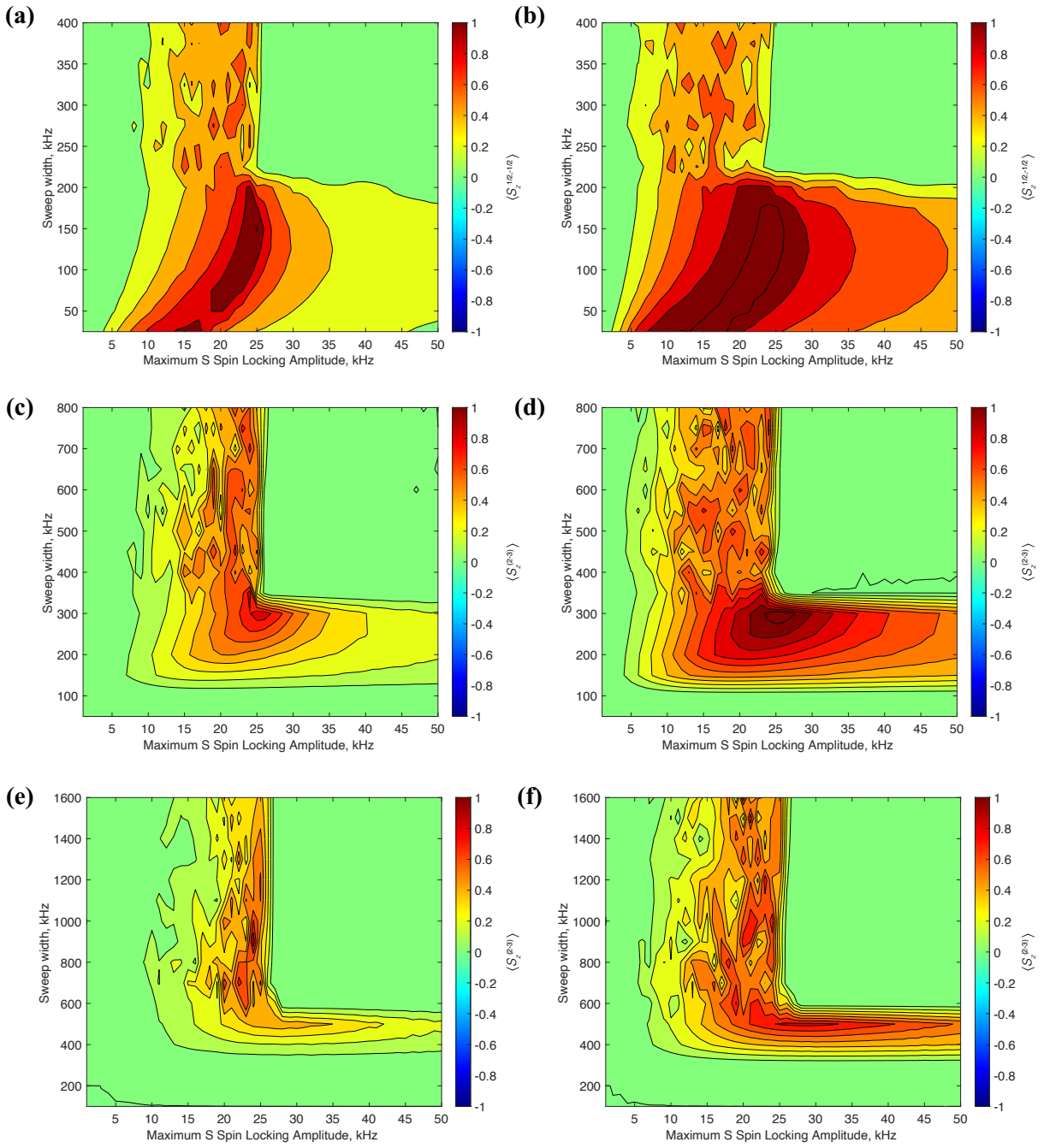

Figure S4: Numerical simulations of $\langle \mathbf{S}_z^{(2\text{-}3)} \rangle$ for the $\beta = \pi/4$ isochromat calculated as a function of spin locking power $\nu_{1,S}$ and sweep width Δ, where values of (a, c, and e) $C_Q(^{35}\text{Cl}) = 6.5$, 9.6, 13.5 MHz and (b, d, f) $C_Q(^{75}\text{As}) = 8.5$, 12.8, 18 MHz are used to generated CT pattern breadths of 100 (a and b), 200 (c and d), and 400 kHz (e and f). In every case, $\eta_Q = 0$, $\nu_{1,I} = 50$ kHz, and $\Omega_S/2\pi$ is set to the center of gravity of the powder pattern.

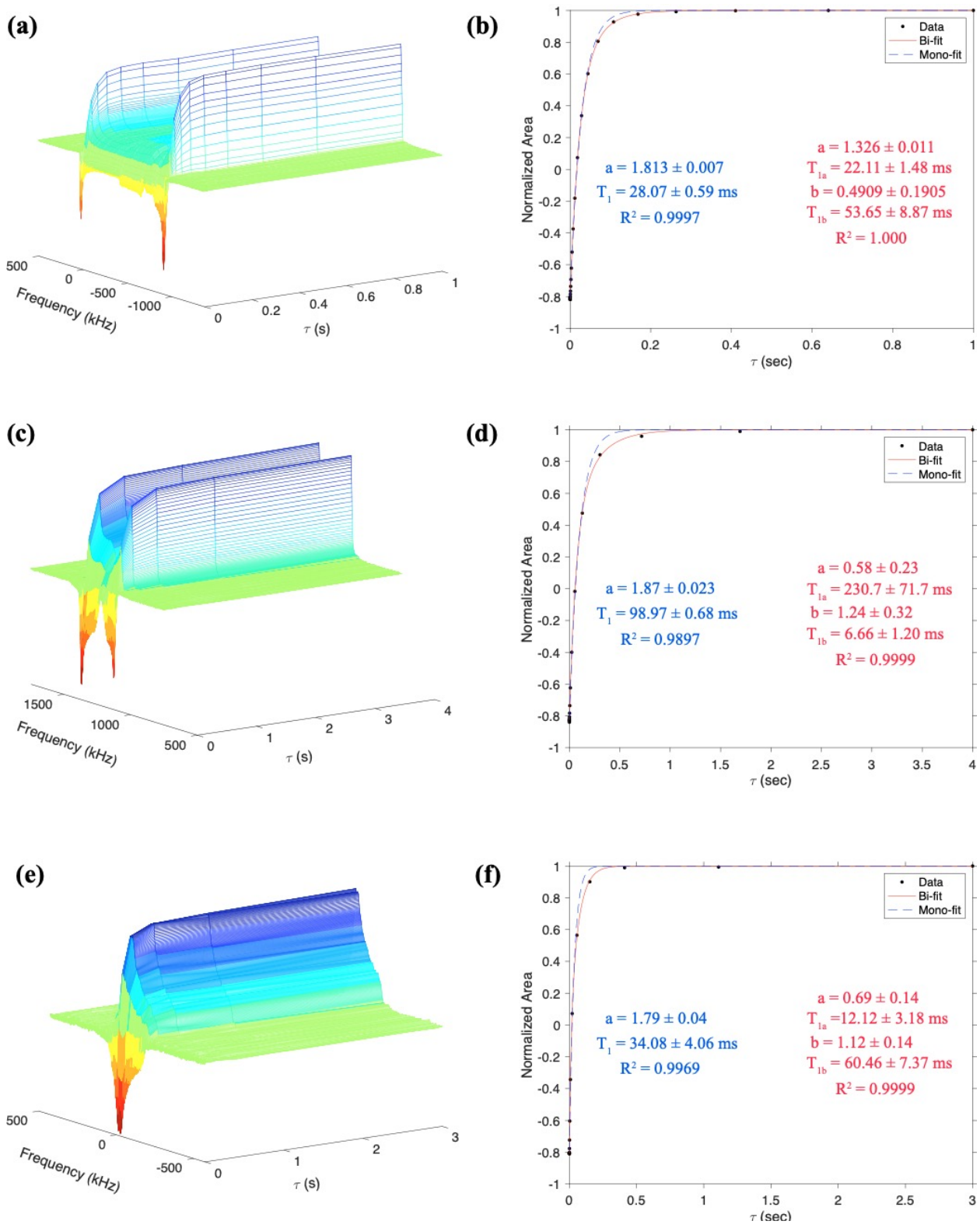

Figure S5: WCPMG-IR T_1 measurements of ^{55}Mn of η^5-CpMn(CO)$_3$ (a and b), ^{59}Co of [Co(NH$_3$)$_5$Cl]Cl$_2$ (c and d), and ^{93}Nb of CpNbCl$_4$ (e and f). SSNMR spectra acquired as a function of the delay time are shown in the left column, and corresponding normalized integrated areas under the powder pattern are fitted with monoexponential and biexponential functions of the form $M_z(t) = 1 - ae^{-\tau/T1a} - b^{-\tau/T1b}$ (where $b = 0$ in the monoexponential case) in the right column.

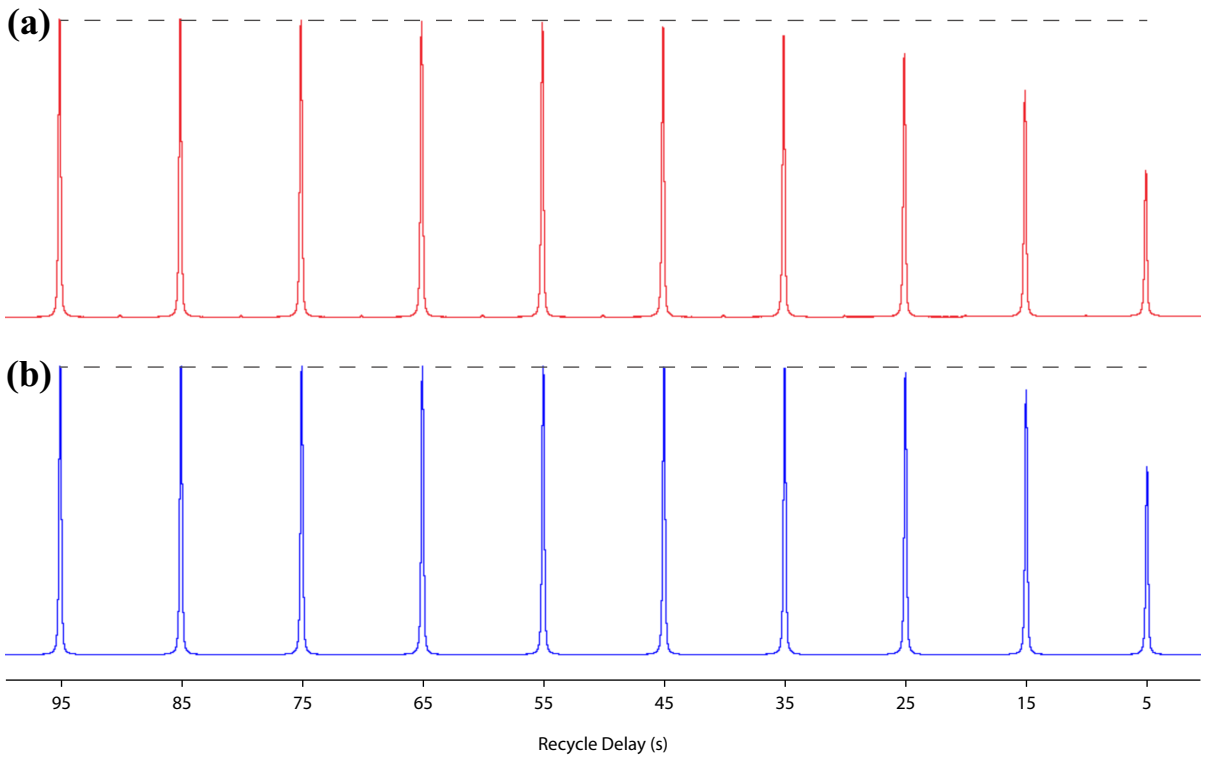

Figure S6: ^{1}H SSNMR spectra of η^5-$C_5H_5Mn(CO)_3$ acquired with a Bloch decay (a) and a Bloch decay followed by a flip-back pulse (b) as a function of decreasing recycle delay time.

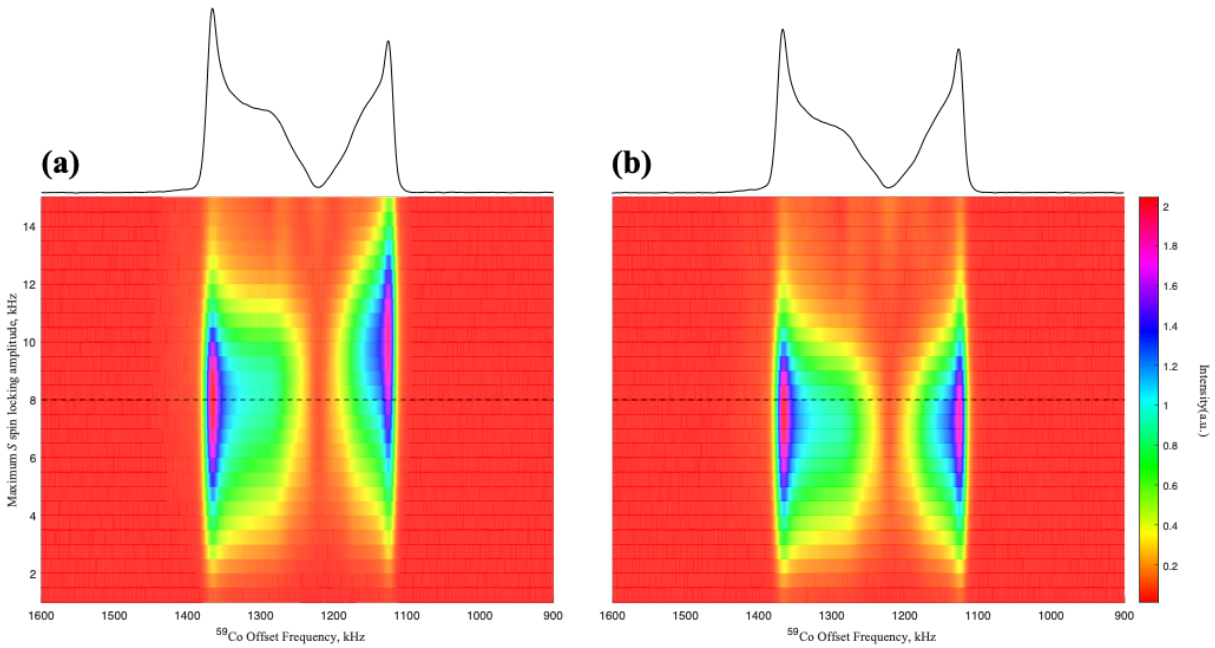

Figure S7: ^{1}H-^{59}Co BRAIN-CP static SSNMR spectra of $[Co(NH_3)_5Cl]Cl_2$ acquired at 14.1 T using (a) a constant ^{1}H spin locking amplitude of 40 kHz and (b) a ramped ^{1}H spin locking amplitude from 28 to 40 kHz. For each case, $\nu_{1,S}$ is arrayed from 1 to 15 kHz in increments of 0.5 kHz. The dashed line at $\nu_{1,S}$ = 8 kHz indicates the best matching conditions which result in the most uniform powder pattern of the highest signal intensity, which is displayed above each contour plot.

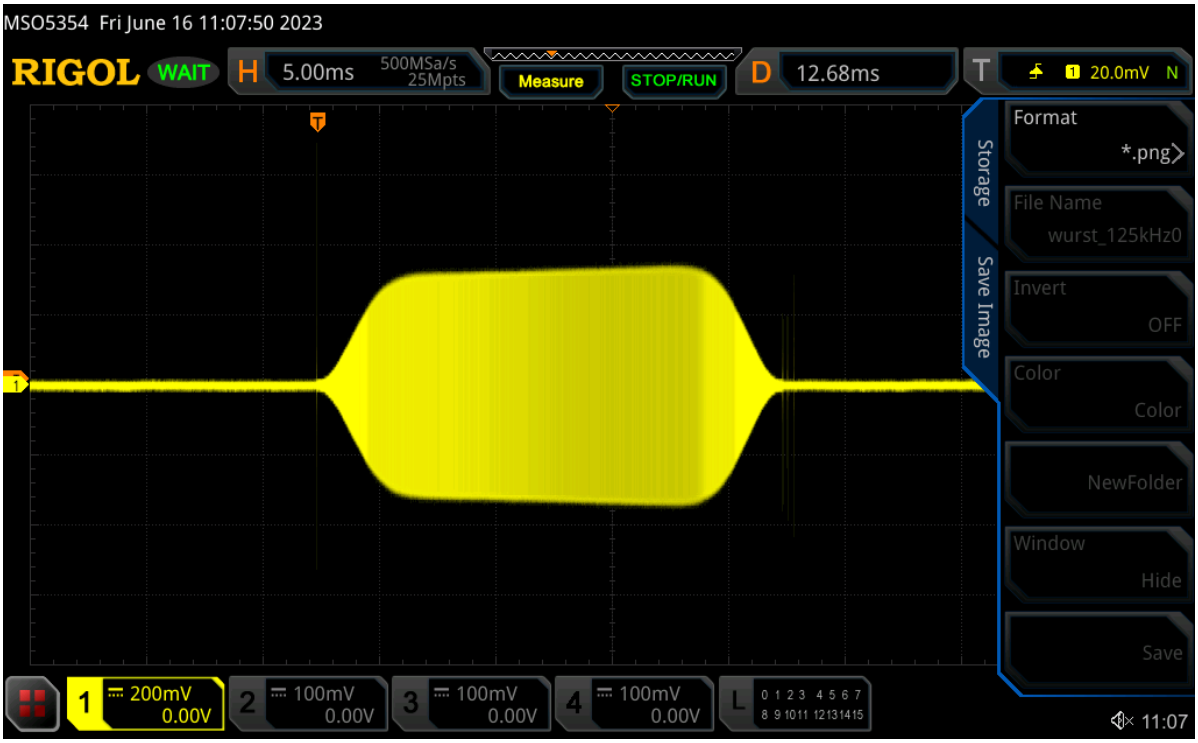

Figure S8: Oscilloscope image of a WURST pulse at ω_0 = 148.735 MHz using a home-built 5 mm double resonance probe with Δ = 125 kHz.

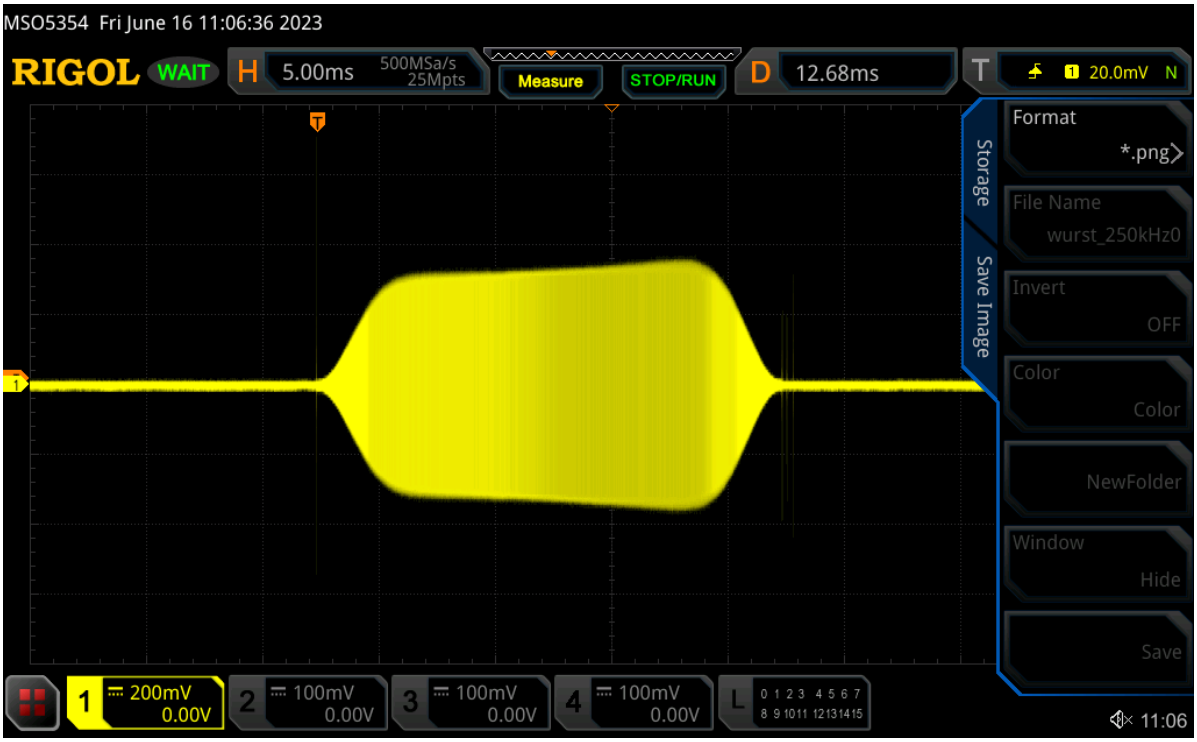

Figure S9: Oscilloscope image of a WURST pulse with Δ = 250 kHz

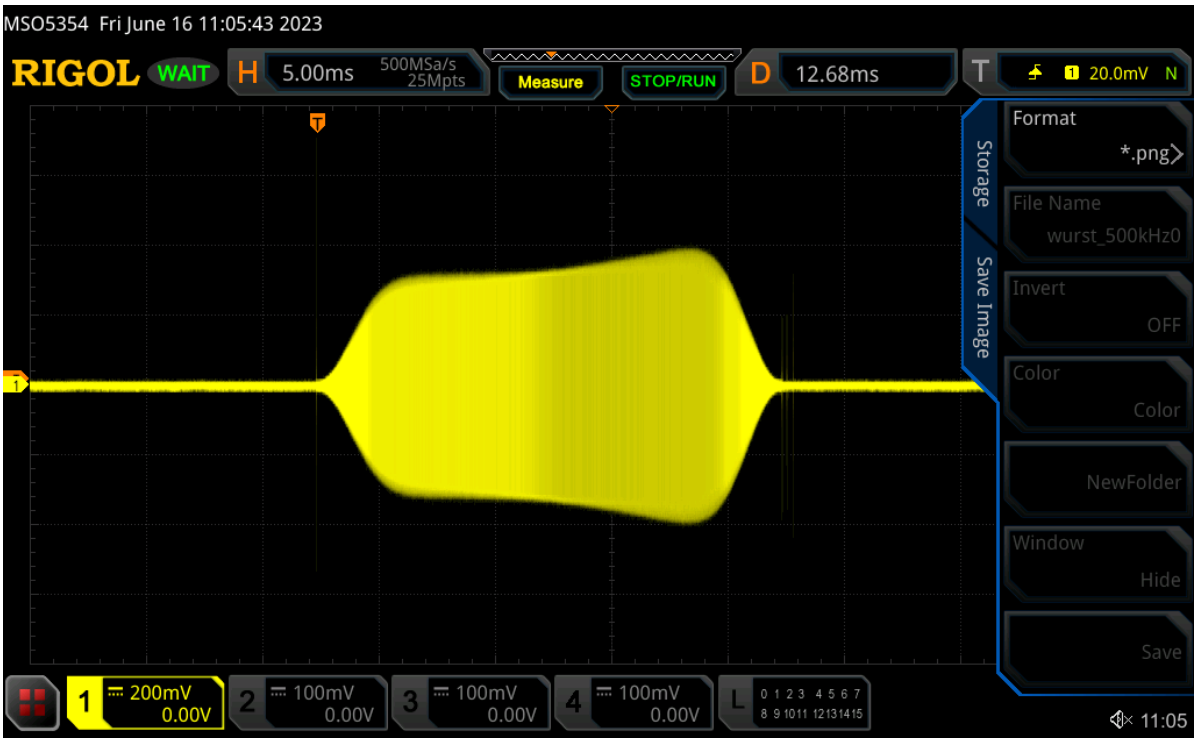

Figure S10: Oscilloscope image of a WURST pulse with Δ = 500 kHz

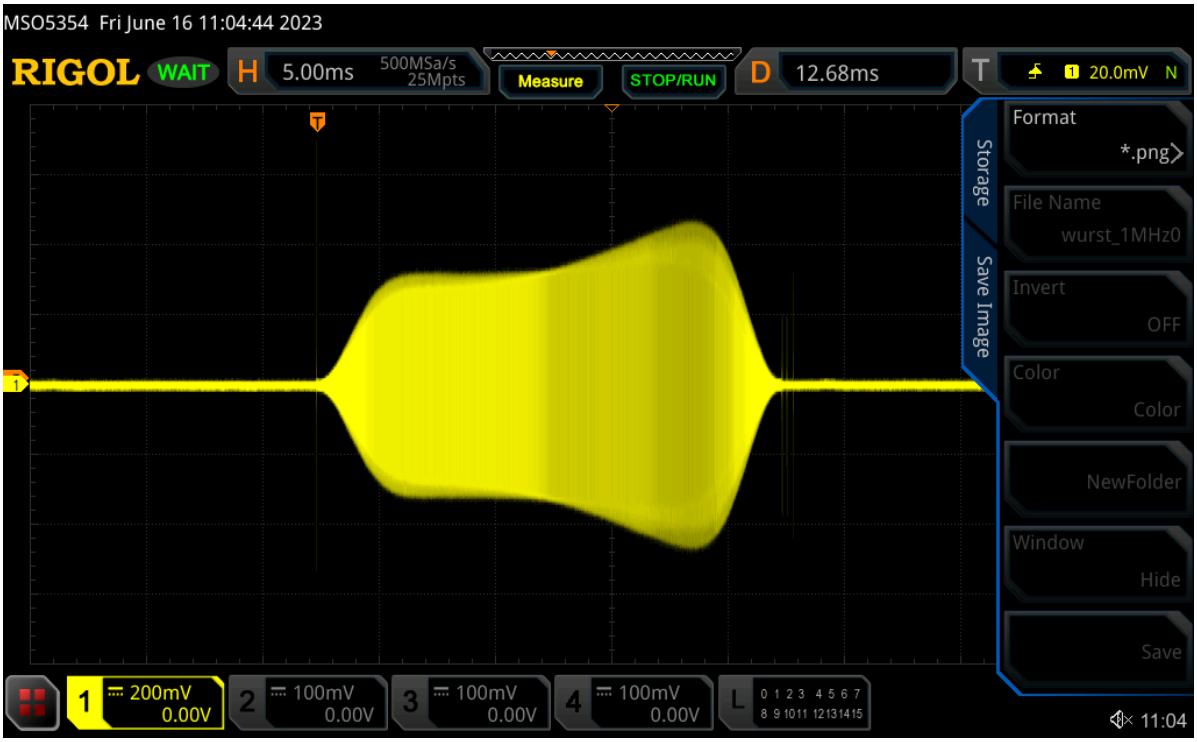

Figure S11: Oscilloscope image of a WURST pulse with Δ = 1 MHz

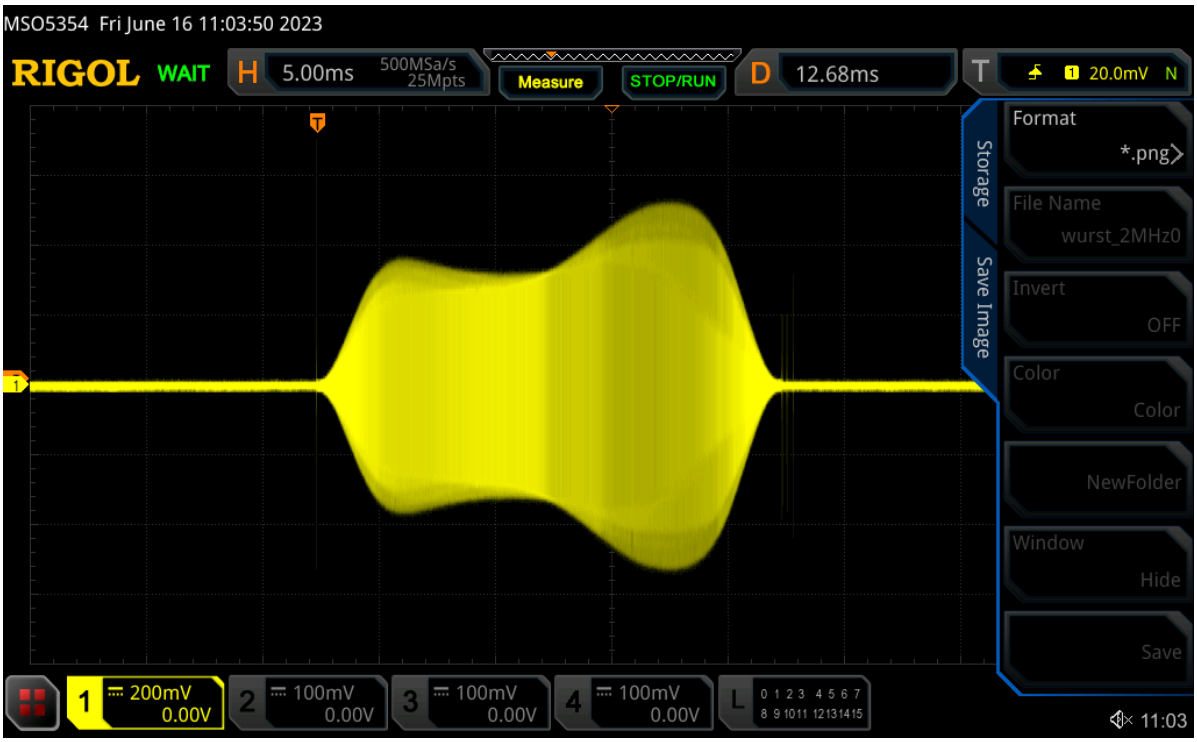

Figure S12: Oscilloscope image of a WURST pulse with Δ = 2 MHz

(1) Altenhof, A. R.; Gan, Z.; Schurko, R. W. *J. Magn. Reson.* **2022**, *337*, 107174.
(2) Baum, J.; Tycko, R.; Pines, A. *Phys. Rev. A* **1985**, *32*, 3435–3447.
(3) O'Dell, L. A. *Solid State Nucl. Magn. Reson.* **2013**, *55–56*, 28–41.
(4) Garwood, M.; DelaBarre, L. *J. Magn. Reson.* **2001**, *153*, 155–177.
(5) Vega, S. *J. Chem. Phys.* **1978**, *68*, 5518–5527.
(6) Vega, S. *Phys. Rev. A* **1981**, *23*, 3152–3173.
(7) Harris, K. J.; Lupulescu, A.; Lucier, B. E. G.; Frydman, L.; Schurko, R. W. *J. Magn. Reson.* **2012**, *224*, 38–47.
(8) Rovnyak, D. *Concepts Magn. Reson. Part A Bridg. Educ. Res.* **2008**, 254–276.
(9) Amoureux, J. P.; Pruski, M. *Mol. Phys.* **2002**, *100*, 1595–1613.
(10) Ashbrook, S. E.; Wimperis, S. *Mol. Phys.* **2000**, *98*, 1–26.
(11) Altenhof, A. R.; Lindquist, A. W.; Foster, L. D. D.; Holmes, S. T.; Schurko, R. W. *J. Magn. Reson.* **2019**, *309*, 106612.
(12) Koppe, J.; Hansen, M. R.; Hansen, M. R. *J. Phys. Chem. A* **2020**, *124*, 4314–4321.